SCIENCE ADVANCES | RESEARCH ARTICLE

APPLIED PHYSICS

High-frequency cavity optomechanics using bulk acoustic phonons

Prashanta Kharel[1]*, Glen I. Harris[2], Eric A. Kittlaus[1], William H. Renninger[1], Nils T. Otterstrom[1], Jack G. E. Harris[2], Peter T. Rakich[1]*

To date, microscale and nanoscale optomechanical systems have enabled many proof-of-principle quantum operations through access to high-frequency (gigahertz) phonon modes that are readily cooled to their thermal ground state. However, minuscule amounts of absorbed light produce excessive heating that can jeopardize robust ground-state operation within these microstructures. In contrast, we demonstrate an alternative strategy for accessing high-frequency (13 GHz) phonons within macroscopic systems (centimeter scale) using phase-matched Brillouin interactions between two distinct optical cavity modes. Counterintuitively, we show that these macroscopic systems, with motional masses that are 1 million to 100 million times larger than those of microscale counterparts, offer a complementary path toward robust ground-state operation. We perform both optomechanically induced amplification/transparency measurements and demonstrate parametric instability of bulk phonon modes. This is an important step toward using these beam splitter and two-mode squeezing interactions within bulk acoustic systems for applications ranging from quantum memories and microwave-to-optical conversion to high-power laser oscillators.

INTRODUCTION

The coherent control of mechanical objects (*1*–*4*) can enable applications ranging from sensitive metrology (*5*) to quantum information processing (*6*, *7*). An array of devices (*8*–*14*) ranging from nano-optomechanical crystals to suspended micromirrors have been used to manipulate mechanical degrees of freedom using light. Central to the field of cavity optomechanics—and more generally to quantum information science—is the ability to harness long-lived mechanical excitations at high frequencies (*15*). Long-lived high-frequency phonons can be initialized deep in their quantum ground states and can preserve coherent information for extended periods of time in the presence of various decoherence channels. Optomechanical systems using high-frequency (gigahertz) phonons have enabled ground-state cooling (*16*), quantum control at the single-phonon level (*17*, *18*), and remote entanglement between mechanical resonators (*19*–*21*). However, it may be difficult to implement more sophisticated quantum protocols using these systems because of spurious forms of laser heating that threaten robust ground-state operation within microscale and nanoscale systems (*16*, *18*, *22*). New device strategies may be necessary to mitigate these decoherence mechanisms for robust quantum optical control of high-frequency phonons.

Efficient optomechanical coupling to high-frequency bulk acoustic waves within macroscopic systems offers an alternative path to robust quantum control of phonons. Optical access to these phonons within pristine crystalline solids yield greatly reduced surface interactions and favorable thermal characteristics to mitigate spurious laser heating (*23*, *24*). These resonators also grant access to world-record $f \cdot Q$ products (*23*), a key figure of merit that characterizes decoupling of a resonator from its thermal environment (*15*). While these bulk acoustic phonon modes have been accessed through Brillouin-like coupling using a free-space laser beam (*24*, *25*), new strategies are needed to translate this physics into cavity optomechanical systems as the basis for phonon counting (*17*, *26*), generation of nonclassical mechanical states (*18*), and efficient transduction of information between optical and phononic domains (*27*).

Here, we realize a cavity-optomechanical system that harnesses high-frequency (13 GHz) bulk acoustic phonon modes within a macroscopic crystal, offering an array of properties that open the door to robust quantum manipulation of phonons. These high-frequency phonons, with large (20 μg) motional masses, are used to mediate resonant coupling between two distinct modes of an optical cavity through Brillouin interactions. To enable beam splitter and entanglement interactions as the basis for quantum optical control of phonons, we engineer the multimode spectrum of the optical cavity to break the symmetry between the Stokes and anti-Stokes processes while allowing resonant driving of a chosen optical mode. Resonant driving allows us to attain intracavity photon numbers that are more than six orders of magnitude larger than those of high-frequency microscale counterparts (*16*). These resonantly enhanced photon numbers permit large (megahertz) optomechanical coupling rates and greater than unity cooperativities, necessary for efficient control of phonons using light. In addition, we demonstrate that phase-matched Brillouin interactions produce controllable coupling to one or more phonon modes, opening the door to new forms of multimode entanglement (*28*). Looking beyond the field of cavity quantum optomechanics, this device strategy presents new opportunities for sensitive materials spectroscopy and oscillator technologies.

Bulk crystalline optomechanical system

In what follows, we explore optomechanical interactions mediated by macroscopic phonon modes within the bulk crystalline cavity optomechanical system of Fig. 1A. A 5.2-mm-thick flat-flat quartz crystal is placed within a nearly hemispherical Fabry-Pérot cavity having high-reflectivity (98%) mirrors; this optomechanical assembly is cooled to ~8 K temperatures to greatly extend the phonon lifetimes within crystalline quartz. At room temperature, high-frequency phonons (>10 GHz) have a mean free path (~100 μm) that is much smaller than the crystal dimension. Just as the optical Fabry-Pérot resonator supports a series of standing electromagnetic waves (red and

---

[1]Department of Applied Physics, Yale University, New Haven, CT 06511, USA. [2]Department of Physics, Yale University, New Haven, CT 06520, USA.
*Corresponding author. Email: prashanta.kharel@yale.edu (P.K.); peter.rakich@yale.edu (P.T.R.)

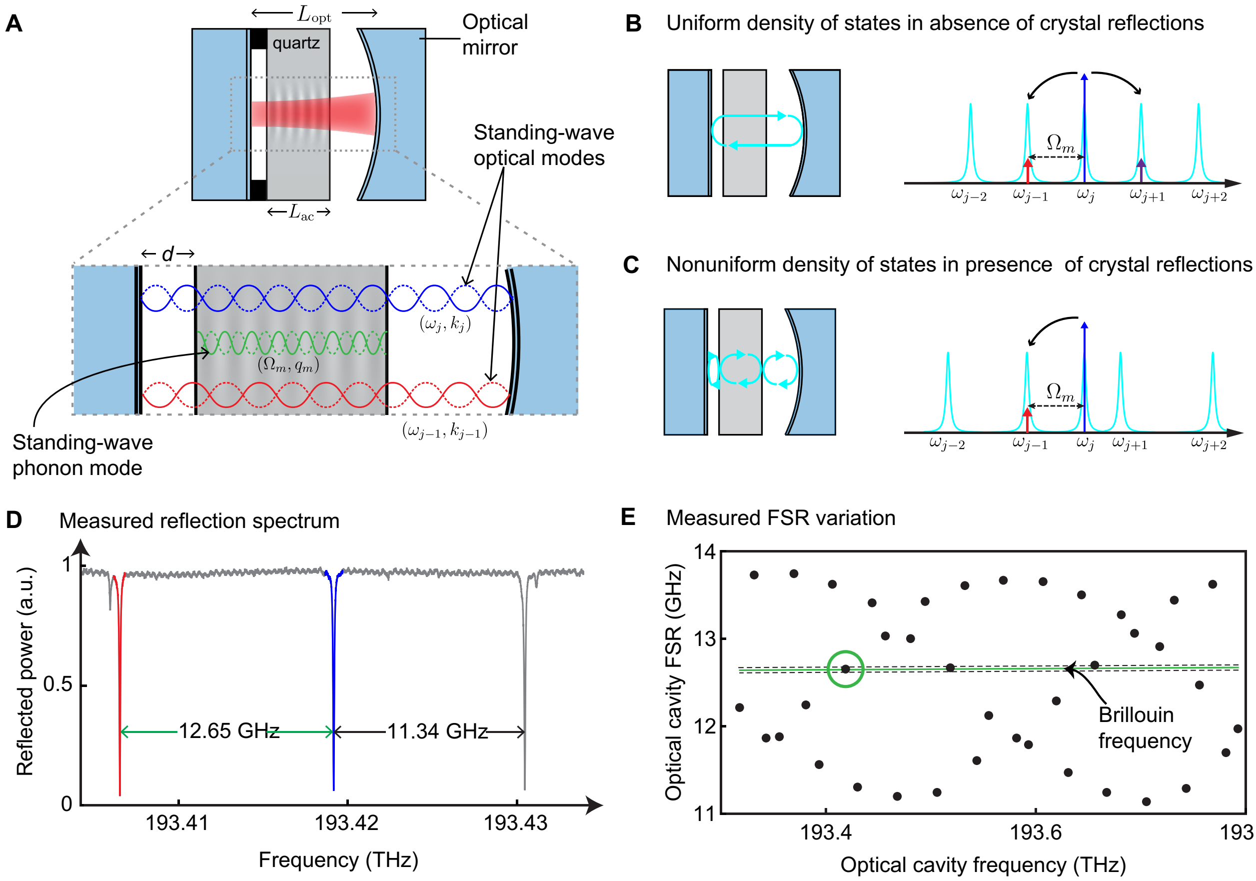

Fig. 1. The multimode cavity optomechanical system. (**A**) Schematic of an optomechanical system that consists of a bulk acoustic wave resonator that is placed inside an optical cavity. Two distinct standing-wave longitudinal optical modes interact through electrostrictive coupling with a standing-wave longitudinal phonon mode formed within the planar crystalline quartz crystal at cryogenic temperatures (~8 K). Large mode volumes for both light and sound result from macroscopic geometrical parameters: $L_{\text{ac}} \simeq 5.2$ mm, $L_{\text{opt}} \simeq 9.1$ mm, and $d \simeq 0.15$ mm. (**B**) Assuming no optical reflections in the quartz-vacuum interface, one obtains equally spaced longitudinal optical modes. Therefore, a phonon mode mediating intermodal optomechanical interactions can scatter incident laser light at ω_j to adjacent optical modes ω_{j+1} and ω_{j-1} with nearly equal scattering rates. (**C**) However, modest optical reflections (~4%) in the quartz-vacuum interface, which lead to notable non-uniformity in optical mode spacing, can be exploited to bias our system to strongly favor one scattering process ($\omega_j \rightarrow \omega_{j-1}$) over the other ($\omega_j \rightarrow \omega_{j+1}$). The variation in cavity resonances arises because of dispersive shifts of cavity resonances arising from multipath interference. (**D**) The reflection spectrum of the optical cavity obtained by frequency sweeping an incident laser light reveals this variation in optical mode spacing (or FSR) between adjacent fundamental Gaussian modes. a.u., arbitrary units. (**E**) Measurement of the FSR over a wider frequency range by sweeping the laser from 1548- to 1552-nm wavelength shows large undulation (2.6 GHz) in the FSR as a function of the optical cavity frequency. Consequently, we find multiple pairs of resonances with frequency differences that are equal to the Brillouin frequency, which is a necessary requirement for intermodal optomechanical coupling in our system.

blue) seen in Fig. 1A, the planar surfaces of the quartz crystal produce acoustic reflections to form an acoustic Fabry-Pérot resonator that supports a series of standing-wave elastic modes (green) at these low temperatures. To avoid anchoring losses, an annular spacer prevents the crystal surface from contacting the mirror; this same spacer sets the position of the crystal (d) within the cavity.

These high-frequency bulk acoustic phonon modes are used to mediate efficient coupling between distinct longitudinal optical modes of the Fabry-Pérot cavity through a multiresonant (or multimode) optomechanical process. Coupling occurs through a Brillouin-like optomechanical process when the time-modulated electrostrictive optical force distribution, produced by the interference between distinct modes of the Fabry-Pérot cavity, matches the elastic profile (and frequency) of a bulk acoustic phonon mode. The same intrinsic photoelastic response that generates the optical forces within the crystal also modulates the refractive index of the crystal via elastic-wave motion. Through the formation of a time-modulated photoelastic grating, these "Brillouin-active" elastic waves mediate dynamical Bragg scattering (or energy transfer) between distinct longitudinal modes of the optical Fabry-Pérot cavity.

Because of the extended nature of the optomechanical interaction within the crystal, phase matching and energy conservation determine the set of phonon modes (Ω_m, q_m) that can mediate resonant coupling between adjacent optical modes (ω_j, k_j) and (ω_{j-1}, k_{j-1}) of the Fabry-Pérot cavity (see Fig. 1A). One finds that the Brillouin-active phonons must satisfy the conditions $q_m = k_{j-1} + k_j$ and $\Omega_m = \omega_j - \omega_{j-1}$ to mediate dynamical Bragg scattering within the crystal. Neglecting some details pertaining to modal overlaps, one expects that phonons in a narrow band of frequencies near the Brillouin frequency ($\Omega_B \simeq 2\omega_j \upsilon_a / \upsilon_o$) can meet this condition; here, $\upsilon_a(\upsilon_o)$ is the speed of sound (light) in the quartz crystal. Within the z-cut crystalline quartz substrate, this expression leads us to expect intermodal coupling at $\Omega_B \simeq 2\pi \times 12.7$ GHz when driving the optical cavity with 1.55-μm wavelength light. On the basis of the resonance condition, we seek a Fabry-Pérot design whose free spectral range (FSR), defined as $\omega^{j}_{\rm FSR} = \omega_j - \omega_{j-1}$, matches the Brillouin frequency Ω_B.

Most applications of optomechanical interactions require a means of selecting between the Stokes and anti-Stokes interactions. Conventional single-mode cavity optomechanical systems use the detuning of an external drive field from a single-cavity resonance to produce this asymmetry. By comparison, this multimode system offers the possibility for resonant pumping, which carries many advantages (see Discussion). However, in the case when the optical Fabry-Pérot resonator has regular mode spacing (i.e., $\omega^{j}_{\rm FSR} = \omega^{j-1}_{\rm FSR}$), resonant driving of the optical cavity presents a problem; a Brillouin-active phonon mode (Ω_m) that matches the multimode resonant condition will resonantly scatter incident photons of frequency ω_j to adjacent cavity modes ω_{j-1} and ω_{j+1} with nearly equal probabilities (see Fig. 1B).

The introduction of the quartz crystal into the optical Fabry-Pérot resonator provides an elegant means of solving this problem; modest optical reflections (~4%) produced by the surfaces of the crystal shift the modes of the Fabry-Pérot cavity. As a result, the typically uniform density of modes (Fig. 1B) is transformed into a highly nonuniform density of modes (Fig. 1C) such that $\omega^{j}_{\rm FSR} \neq \omega^{j-1}_{\rm FSR}$. Using this strategy, we are able to choose between the Stokes ($\omega_j \to \omega_{j-1}$) and anti-Stokes ($\omega_{j-1} \to \omega_j$) processes with high selectivity, even when the external drive field is directly on resonance. For example, Fig. 1C illustrates how a dispersively engineered mode spacing ($\omega^{j}_{\rm FSR} \neq \omega^{j-1}_{\rm FSR}$) permits us to bias the system for Stokes scattering with resonant optical driving at frequency ω_j.

This modification to the density of modes can be seen from reflection measurements of this bulk crystalline optomechanical system (Fig. 1D), which reveal a large (~21%) undulation in the FSR of the optical Fabry-Pérot resonator; Fig. 1E shows the measured frequency spacing between adjacent optical resonances ($\omega^{j}_{\rm FSR} = \omega_{j+1} - \omega_j$) when an incident laser field is mode-matched to the fundamental Gaussian mode of the cavity. The observed variation in optical FSR agrees well with scattering matrix treatments of the system (see section S1). The large spread in mode separations makes it straightforward to find pairs of optical modes whose frequency difference satisfies the multimode resonance condition. Within the measurements of Fig. 1E, one can readily identify three sets of modes (green) that satisfy this condition. Moreover, this dispersive shift permits us to fine-tune the FSR of a given mode pair to match Brillouin frequency through a small (<1 K) change in temperature (see section S1).

Even with resonant driving of the optical mode, this form of symmetry breaking results in a large (>1000-fold) difference between the Stokes and anti-Stokes scattering rates. In conventional single-mode cavity optomechanical systems, this large Stokes/anti-Stokes asymmetry is produced by far-detuning the drive from an optical cavity at the expense of the intracavity photon number. In contrast, this multimode optomechanical system permits greatly enhanced intracavity photon numbers for the same input power through resonant driving (*29*). The relative strength of the Stokes/anti-Stokes scattering rates in the case of resonant driving is determined by the ratio $(2\Delta\omega/\kappa)^2$, where $\Delta\omega = \omega^{j+1}_{\rm FSR} - \omega^{j}_{\rm FSR}$ is the difference in the FSR between adjacent optical modes and κ is the optical mode linewidth (see section S7). Because $\Delta\omega$ is well resolved from the linewidth (i.e., $2\Delta\omega/\kappa \simeq 36$), we can virtually eliminate the Stokes or anti-Stokes interaction by resonantly exciting an appropriately chosen mode.

The multimode coupling described above can be represented by the interaction Hamiltonian $H^{m}_{\rm int} = -\hbar g^{m}_{0}\left(a^{\dagger}_{j+1} a_j b_m + a^{\dagger}_{j} a_{j+1} b^{\dagger}_{m}\right)$ (*30*). Here, $a^{\dagger}_{j}$ is the creation operator for the optical mode at frequency ω_j, $b^{\dagger}_{m}$ is the creation operator for the phonon mode at frequency Ω_m, and g^{m}_{0} is the single-photon coupling rate that characterizes the strength of the optomechanical interaction (see section S2, A to C). This single-photon coupling rate describes the change in the frequency spacing between the two optical modes resulting from the dynamical modulation of the refractive index of the crystal. Because the acoustic FSR ($\upsilon_a/2L_{\rm ac}$) of the bulk acoustic waves within our quartz substrate is much smaller than the optical linewidth ($\kappa/2\pi$), more than one phonon mode (Ω_m) near the Brillouin frequency (Ω_B) can participate in the optomechanical coupling. Hence, the total interaction Hamiltonian, which includes contributions from all these phonon modes, becomes $H_{\rm int} = \sum_m H^{m}_{\rm int}$.

To calculate the single-photon coupling rate, g^{m}_{0}, we consider the interaction energy $H^{\rm int} = -\int_V dV \sigma(\mathbf{r}) \cdot S(\mathbf{r})$ for photoelasticity-mediated coupling between light and sound fields, where $\sigma(\mathbf{r})$ is the electrostrictively induced stress and $S(\mathbf{r})$ is the phonon mode's strain field. For simplicity, we assume coupling between longitudinal phonon modes propagating in the z direction with linearly polarized electromagnetic modes in the x direction. The dominant stress tensor component $\sigma \equiv \sigma_z = -(1/2)\epsilon_0\epsilon^2_r p_{13} E_x(z)^2$, where ϵ_0 (ϵ_r) is the vacuum (relative) permittivity of the optical cavity, p_{13} is the relevant photoelastic constant of the quartz crystal, and E_x is the electric field of the optical cavity mode. Similarly, the dominant strain component $S \equiv S_z = \partial u_z/\partial z$, where u_z is the displacement field of the phonon mode. We use the normal mode expansion of the electric and acoustic displacement fields [i.e., $E_x(z) = \sum_j E_j \sin(k_j z)\left(a_j + a^{\dagger}_{j}\right)$ and $u_z(z) = \sum_m U_m \cos(q_m(z-d))(b_m + b^{\dagger}_{m})$] to obtain the following interaction Hamiltonian in the rotating wave approximation

$$H^{\rm int} = -\sum_{j,j',m} \int dV \epsilon_0 \epsilon^2_r p_{13} q_m U_m E_j E_{j'} \sin(k_j z) \sin(k_{j'} z) \sin(q_m(z-d)) \times \left(a^{\dagger}_{j} a_{j'} b_m + a_j a^{\dagger}_{j'} b^{\dagger}_{m}\right) \quad (1)$$

where $E_j = \sqrt{\hbar\omega_j/(\epsilon_0\epsilon_r V_{\rm opt})}$ $(U_m = \sqrt{\hbar/(\rho V_{\rm ac}\Omega_m)})$ is the zero-point amplitude of the electric (acoustic) field, k_j (q_m) is the optical (acoustic) wave vector of the standing-wave optical (acoustic) mode, $V_{\rm opt}$ ($V_{\rm ac}$) is the effective mode volume of the optical (acoustic) mode, d is the position of the crystal within the optical cavity, and ρ is the mass density of the crystal (see section S2D). Expressing Eq. 1 as $-\sum_m \hbar g^{m}_{0}\left(a^{\dagger}_{j} a_{j'} b_m + a_j a^{\dagger}_{j'} b^{\dagger}_{m}\right)$, we see that the single-photon coupling rate g^{m}_{0} for intermodal optomechanical coupling between two optical modes (ω_j, k_j) and (ω_{j+1}, k_{j+1}) mediated by a phonon mode (Ω_m, q_m) is given by

$$\hbar g^{m}_{0} = \int dV \epsilon_0 \epsilon^2_r p_{13} q_m U_m E_j E_{j'} \sin(k_j z) \sin(k_{j'} z) \sin(q_m(z-d)) \quad (2)$$

Using the parameters of our system, Eq. 2 predicts a maximum single-photon coupling rate of $|g^{m}_{0}| \simeq 2\pi \times 24$ Hz. Note that this coupling rate is produced by a phonon mode with a motional mass of 20 μg, which is 1 million to 100 million times larger than previous gigahertz frequency optomechanical systems (see Materials and Methods) (*12*, *13*, *31*).

The wave vector–selective nature of this coupling enables new approaches to precisely tailor interaction with one or more phonon modes. This system differs from conventional Brillouin scattering because even phonon modes that satisfy both energy conservation and phase-matching requirements can have vanishing optomechanical coupling rates. This intriguing new feature arises because the coupling to a particular phonon mode also depends on the location of the crystal (d) inside the optical cavity. For instance, the overlap integral in Eq. 2 yields a coupling rate of zero when the position of the crystal is such that nodes of a phonon mode coincide with the antinodes of the optical forcing function.

Despite the fact that this current apparatus does not permit us to change the crystal position, we can still control the number of phonon modes that participate in the optomechanical interaction. Independent of crystal location, a pair of adjacent optical modes is guaranteed to couple to at least one phonon mode near the Brillouin frequency because the phase-matching condition is relaxed by the crystal's finite length. However, by using optical resonances at different wavelengths, one can change the position of the nodes inside the crystal, thereby selecting a different group of phonons to mediate optomechanical coupling (see section S2D).

RESULTS

Probing coherent optomechanical response

We explore the optomechanical coupling in our system by probing its coherent response to an optical drive. Specifically, we use the well-known techniques called optomechanically induced amplification (OMIA) and optomechanically induced transparency (OMIT) (*32*).

These measurements are performed using a tunable laser at frequency ω_l, whose output is split into two arms (see Fig. 2A). Laser light in one arm is intensity-modulated at a variable frequency (Ω) using a microwave generator. Light in the other arm is frequency-shifted to $\omega_l + 2\pi \times 44.0$ MHz using an acousto-optic modulator (AOM). This AOM-shifted light acts as a local oscillator (LO) such that the Stokes and anti-Stokes signals appear as distinct tones in the radio-frequency (rf) spectrum analyzer during heterodyne detection. The tones at frequencies ω_l and $\omega_l - \Omega$ serve as control and probe lasers, respectively. The strong control laser (ω_l) drives the higher-frequency optical mode at ω_{j+1}, whereas the weak probe laser ($\omega_p = \omega_l - \Omega$) is swept near the lower-frequency optical mode at ω_j (see inset i of Fig. 2A). The third tone at $\omega_l + \Omega$ is irrelevant, as it is not resonant with the optical cavity modes. Light is delivered to and collected from the optical cavity through a combination of fiber collimators and free-space optics. Light transmitted through the optical cavity is combined with the LO and detected using a photoreceiver, which is connected to an rf spectrum analyzer. This spectrum analyzer monitors the beat note between the transmitted probe laser and the LO by tracking the frequency (Ω) of the microwave generator. Heterodyne detection of the probe light transmitted through the optical cavity provides a direct measurement of the intracavity probe power.

This OMIA measurement (Fig. 2B) reveals a broad optical cavity resonance of linewidth $\kappa_j \simeq 2\pi \times 73$ MHz, consistent with the mirrors' reflectivities. Near the center of the optical resonance, we find three narrow resonances (see inset ii of Fig. 2B) corresponding to phonon modes near the Brillouin frequency of 12.661 GHz. These resonances are equally spaced by ~612 kHz, the expected acoustic FSR $\upsilon_a/2L_{\rm ac}$.This result demonstrates optomechanical coupling to multiple high-frequency longitudinal phonon modes, in a manner consistent with the phase matching described by Eq. 2.

In what follows, we tune the optical wavelength to excite a different pair of optical resonances, ensuring that only a single-phonon mode mediates the optomechanical interaction. A typical OMIA spectrum in which the optomechanical coupling is mediated by a single-phonon mode is shown in Fig. 3A. We perform both OMIA and OMIT measurements to determine the associated single-photon coupling rate and the intrinsic mechanical damping rate. When the system is driven by a strong control laser and a weak probe, we can describe the OMIA (OMIT) phenomena with a linearized interaction Hamiltonian

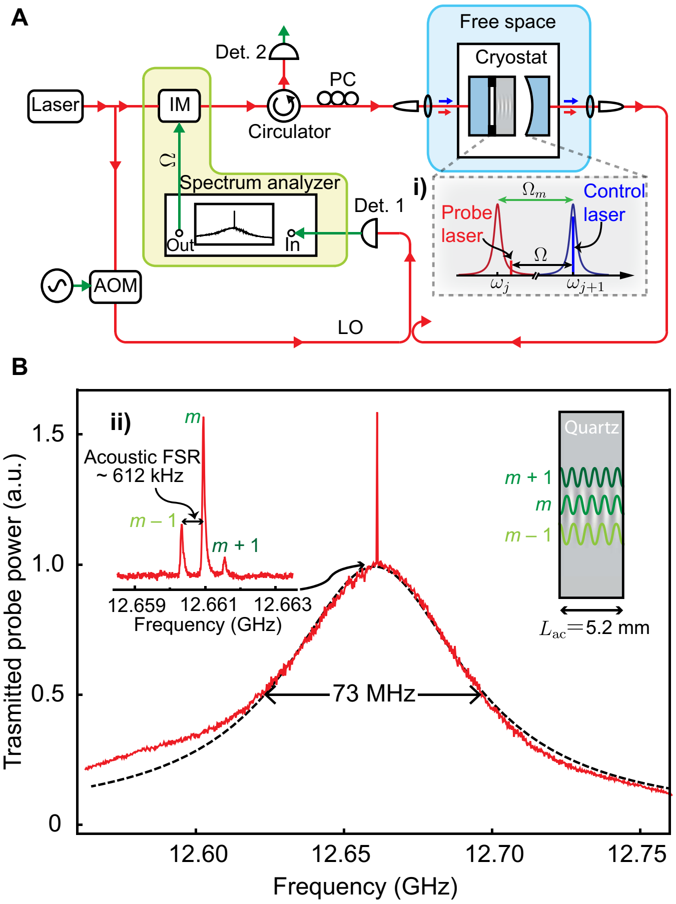

Fig. 2. Optomechanical coupling to a multitude of phonon modes. (**A**) Schematic of the measurement setup used to perform OMIA. A strong control and a weak probe laser are synthesized from the same tunable laser source using an intensity modulator (IM). This light is coupled into and out of the optical cavity using fiber-optic collimators and free-space lenses. The frequency of the tunable laser is set so that the control laser is directly on resonance with the high-frequency optical mode at ω_{j+1} (see inset i). The probe laser is swept near the lower cavity mode at frequency ω_j by sweeping the rf drive frequency (Ω) of the intensity modulator. To examine the coherent response of the intracavity probe field due to optomechanical coupling, a heterodyne measurement is performed between the transmitted probe light and the AOM-shifted laser light. (**B**) We observe coherent buildup of the intracavity photon number as the probe laser is scanned near the optical mode ω_j. The optical cavity decay rate of $\kappa_j \simeq 2\pi \times 73$ MHz obtained for this mode is consistent with the losses at the two mirrors. In addition, we see sharp resonances on the optical mode spectrum corresponding to the phonon-mediated transfer of energy from the high-frequency optical mode at frequency ω_{j+1} to the lower-frequency optical mode at ω_j. A close zoom in of the optical mode spectrum near the center of the optical resonance reveals three high-frequency acoustic modes around 12.661 GHz with a frequency spacing of ~612 kHz (see inset ii). This frequency spacing is consistent with the acoustic FSR of $\upsilon_a/2L_{\rm ac}$ for the standing-wave longitudinal modes formed in crystalline quartz along the z axis. These acoustic modes have very high longitudinal mode numbers (or overtone number) of $m \approx 2.08 \times 10^4$.

$H^m_{\mathrm{int}} = -\hbar g^m_0 \sqrt{n_c}\left(a_j b_m + a^\dagger_j b^\dagger_m\right)$ $\left(H^m_{\mathrm{int}} = -\hbar g^m_0 \sqrt{n_c}\left(a^\dagger_{j+1} b_m + b^\dagger_m a_{j+1}\right)\right)$, where n_c is the intracavity photon number for the optical mode at ω_{j+1} (ω_j). Assuming that the control laser is directly on resonance with the optical mode at ω_{j+1} (ω_j), this effective Hamiltonian predicts a relative OMIA peak height (OMIT dip) of $1/(1 \mp C)^2$, when $\Omega = \Omega_m$. Here, $C = 4n_c|g^m_0|^2/(\kappa\Gamma_m)$ is the cooperativity and Γ_m is the intrinsic mechanical damping rate. Moreover, the linewidth of this OMIA peak (OMIT dip) is given by $\Gamma_{\mathrm{eff}} = (1 \mp C)\Gamma_m$ (*15*).

To measure Γ_m and g^m_0, we varied the control laser power and measured the relative heights and linewidths of the OMIA peaks (OMIT dips) (see Fig. 3, B to G). As expected from theory, the relative heights of the OMIA peaks (OMIT dips) increased (decreased) nonlinearly, whereas the effective linewidth, Γ_{eff}, decreased (increased) linearly as the control laser power was increased from 7.8 to 118 mW. Extrapolating the linear fit in Fig. 3G to zero input power gives $\Gamma_m \simeq 2\pi \times 86$ kHz (acoustic Q factor $\simeq 1.5 \times 10^5$). To understand the acoustic linewidth characteristics, it is useful to view the acoustic propagation within the quartz crystal as being analogous to optical beam propagation within a Fabry-Pérot cavity. This is because the acoustic wavelength (~500 nm) is much smaller than the lateral extent

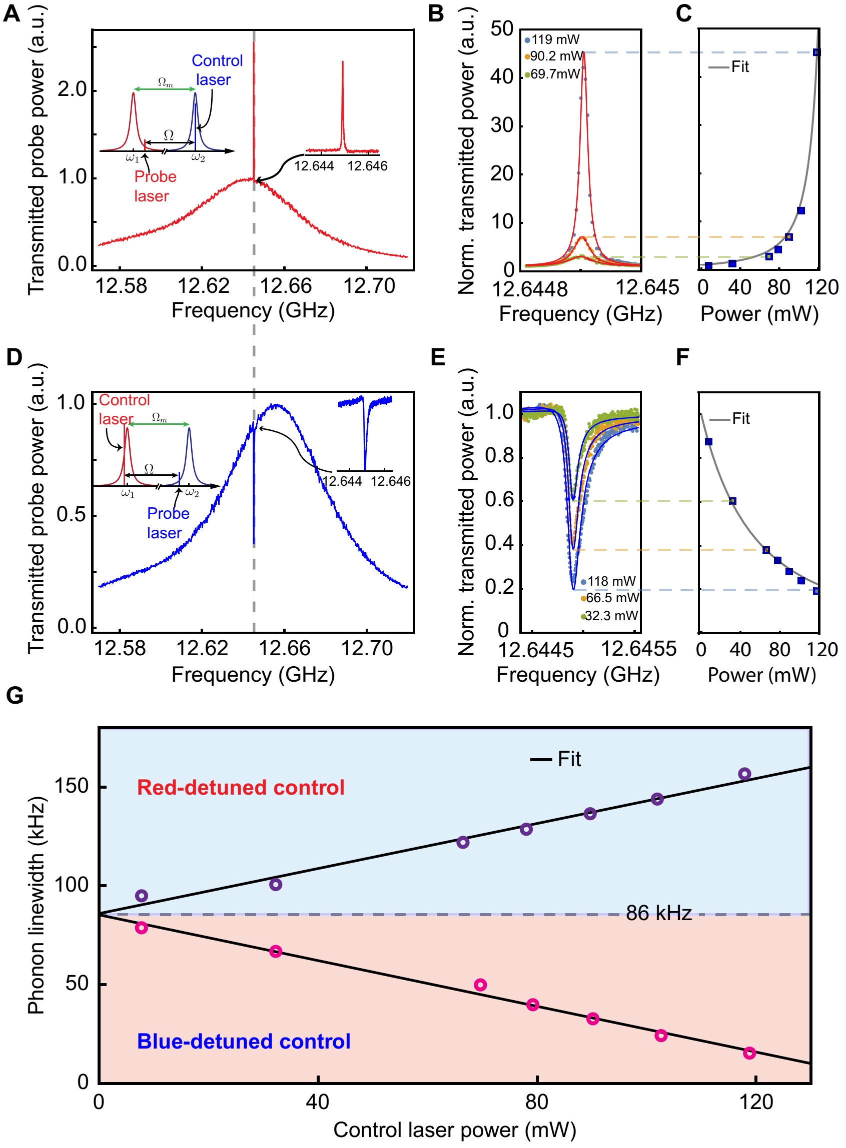

Fig. 3. Characterization of the zero-point coupling rate and the mechanical dissipation rate. (**A**) We perform OMIA measurements on a single-phonon mode using a blue-detuned control laser that is resonant with the high-frequency optical mode (see inset). (**B**) As we increase the power in the control laser, the height of the peak corresponding to the OMIA signal increases nonlinearly with the control laser power, as displayed in (**C**). The linewidth of the OMIA peak, however, decreases with the control power, as seen in (**G**). (**D**) OMIT measurements are performed with the same phonon mode by simply red-detuning the control laser. Note that, because the control laser has a slight offset relative to the low-frequency optical mode at ω_j, the center of the cavity resonance shifts, but the OMIT dip is observed exactly at a phonon frequency of 12.645 GHz. (**E**) The dip of the OMIT signal decreases nonlinearly as a function of the control power, as displayed in (**F**). The linewidth of the OMIT signal, however, increases linearly with the control power, as seen in (G). From the dependence of linewidth as a function of the control laser power, we obtain a cold cavity linewidth $\Gamma_m/2\pi \simeq 86$ kHz for the phonon mode at 12.645 GHz.

of the excited acoustic mode (beam radius ≃ 43 μm) within the crystal. Analogous to diffraction losses within an optical Fabry-Pérot cavity, propagation of a Gaussian acoustic beam within the planar quartz crystal introduces acoustic diffraction losses, which is the dominant source of loss in this present system (see section S5). However, these acoustic *Q* factors can be markedly increased by shaping the surfaces of the quartz crystal to compensate for the effects of diffraction (*24*).

The cooperativities (*C*) and intrinsic mechanical damping rate (Γ_m) obtained from experiments along with n_c calculated from measuring input control laser power P_{in} give $g_0^m \approx 2\pi \times 18$ Hz, consistent with the theoretically predicted maximum value of 2π × 24 Hz (see sections S2 and S3). Note that, based on the measured normalized reflection spectrum (see Fig. 1D) and fraction of light transmitted (85%) on resonance, we assumed critical coupling to the optical mode and negligible internal losses (i.e., $\kappa_i \ll 2\kappa^{\text{ext}}$) while calculating n_c from P_{in}. So far, we have probed the system's coherent response. Next, we explore thermal fluctuations of the phonon mode and self-sustained oscillations (*15*) as we increase the cooperativity to greater than unity.

Thermal fluctuations and phonon self-oscillation

We measure thermal fluctuations of the mechanical mode through spontaneous light-scattering measurements. We use a control laser that is resonant with the higher-frequency optical mode ω_{j+1} (see Fig. 4A); no probe field is supplied for these measurements. The thermally populated phonon mode mediates scattering of incident control photons from frequency ω_{j+1} to ω_j through the Stokes process. Heterodyne detection is used to monitor the power spectrum of this spontaneously scattered Stokes light, as shown in the inset i of Fig. 4B. As the control laser power is increased, we observe a sharp increase in the magnitude of the scattered Stokes light accompanied by spectral narrowing of the heterodyne beat tone (inset ii of Fig. 4B). Optomechanical systems in the blue-detuned regime display these lasing transitions at $C = 1$, when $\Gamma_{\text{eff}} = \Gamma_m(1 - C) = 0$. When $\Gamma_{\text{eff}} < 0$ (i.e., $C > 1$), parametric instability initially causes thermal fluctuations to grow exponentially in time and eventually saturate to reach coherent self-sustained oscillations. This phenomenon is well studied in many optomechanical systems (*29*, *33*) and is also commonly known as "phonon lasing" (*15*). The measurement of total backscattered light from the cavity using a power meter as a function of the input control laser power (Fig. 4B) reveals a self-oscillation threshold of 137 mW, consistent with the threshold (~140 mW) predicted from the measured values of n_c, g_0^m, κ, and Γ_m. The total output Stokes power after lasing is consistent with a slope efficiency of 62% (see section S6A). Note that the intracavity photon number $n_c \approx 6.3 \times 10^9$ is achieved for the highest available control laser power of 204 mW. Such a large intracavity photon number produces cavity-enhanced coupling rate of $g_m = \sqrt{n_c} g_0^m = 2\pi \times 1.5$ MHz and $C = 1.4$. This coupling rate is already more than 10 times larger than Γ_m, as required for high-fidelity transduction of quantum information from the optical to the mechanical domain (or vice versa) (*27*). Last, we note that, although the low signal-to-noise ratio prevented us from measuring thermal fluctuations using a red-detuned drive, these measurements can be readily performed by improving the finesse of the optical cavity (*34*).

DISCUSSION

These results lay the foundation for a promising new class of macroscopic cavity optomechanical systems that rely on bulk acoustic modes of a crystalline solid—rather than subwavelength structural control—to achieve high-frequency multimode interactions. Because phase matching determines the phonon frequency, this approach permits coupling to massive (20 μg), high-frequency phonon modes without size reduction. Resonant optical driving of this multimode system produces appreciable coupling rates (1.5 MHz) to high-frequency (13 GHz) phonons and $C > 1$. These results are obtained using the simplest of flat-flat crystal geometries, meaning that these same principles can be readily used to transform practically any transparent crystal into a high-frequency cavity optomechanical system. Because the Brillouin frequency depends on the optical wavelength and material parameters, these same strategies can be used to harness phonons over a tremendous range of frequencies (e.g., 5 to 100 GHz) by designing the system around different wavelengths and materials. The versatility and robustness of this strategy should lend itself to new types of hybrid

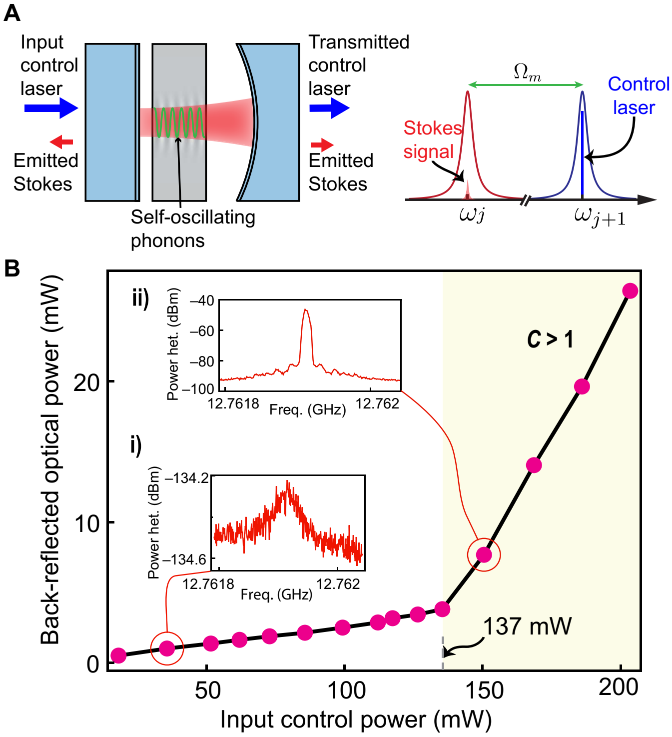

Fig. 4. Thermal fluctuations and regenerative self-oscillations of a high-frequency phonon mode. (**A**) To observe thermal fluctuations of the phonon mode, we turn off the probe laser and tune a strong control laser directly on resonance with the high-frequency optical mode. The thermally populated phonon mode spontaneously scatters light from the higher-energy optical mode to the lower-energy optical mode (Stokes field); this light exits our optical system through both mirrors. (**B**) From the measurement of back-reflected optical power as a function of the input control laser power, we observe a clear threshold behavior at 137 mW corresponding to regenerative self-oscillation of the phonon mode (i.e., $C = 1$). Before threshold, a small (~2.6%) back-reflection results from imperfect coupling of the control laser to the optical mode at ω_2. However, once self-oscillating, phonons scatter a large fraction of the input control laser into the Stokes light, which exits the optical cavity through both forward and backward directions, a substantial increase in the back-reflected optical power occurs. Furthermore, from the heterodyne beat tone of the scattered Stokes light with the frequency-shifted version of the input control laser, we observe a dramatic line narrowing of phonons as we cross the lasing threshold, as displayed in insets i and ii.

quantum systems, new forms of materials spectroscopy, and studies of laser-oscillator physics.

Our quartz-based optomechanical system has many promising features in the context of cavity quantum optomechanics. Large optomechanical coupling rates (>60 MHz) to these high-frequency phonons could be achieved even without miniaturization because this macroscopic system can store a large number of intracavity photons ($>10^{13}$) through resonant driving (*35*). The demonstrated coupling rate of 1.5 MHz is already large enough to enter the strong-coupling regime ($g_m > \kappa/2, \Gamma_m/2$) if the optical finesse is boosted from its current value ($\mathcal{F} \approx 170$) to $\mathcal{F} \approx 10^4$. In this regime, one can deterministically swap excitations between the optical and phononic domains for quantum transduction and the creation of nonclassical mechanical states (*15*). Moreover, because of the potential for reduced thermal decoherence and the opportunity to reach phonon counting sensitivities of less than one, this system shows great promise as a platform to implement probabilistic schemes for quantum-state preparation (see section S8). Owing to the low (high) optical absorption (thermal conductivity) of pristine crystalline quartz [<4.3 dB/km (*36*)] and greatly reduced ($<10^{-4}$) photon-surface interactions relative to high-frequency microscale counterparts (*12*), this system offers a promising path to robust quantum optomechanics.

Hybrid quantum systems using long-lived phonons within bulk acoustic resonators could be a valuable resource for quantum information processing. It is possible to increase the Q factor of these high-frequency phonons within quartz from their present values (1.5×10^5) to 4×10^7 by shaping the acoustic resonator into a plano-convex geometry (*24*). These highly coherent bulk acoustic modes could then be useful as quantum memories. Moreover, these high-Q phonon modes could readily permit strong coupling to individual defect centers for quantum information processing (see section S5), a result that is perhaps surprising given the large acoustic mode volumes relative to previous proposals (*37*, *38*). Simultaneous optomechanical and electromechanical control of bulk acoustic wave phonons within piezoelectric crystals also offers a path toward high-fidelity microwave-to-optical conversion (*39*, *40*).

Beyond the conventional goals of quantum optomechanics, this optomechanical system presents new opportunities for materials spectroscopy and precision measurement. Sensitive metrology of cryogenic phonon physics and defect centers can be performed in a wide array of materials to understand various decoherence channels for phonons. Moreover, bulk acoustic resonators show great potential for quantum noise–limited optomechanical oscillators with ultranarrow fundamental linewidth (<1 nHz) as they can support large coherent phonon populations ($>10^{12}$) (see section S6). These highly coherent oscillators could be used for precision sensing (*41*), time keeping (*42*), and the exploration of new physics (*43*).

MATERIALS AND METHODS

The planar crystalline z-cut α-quartz crystal (Aa grade) used for this experiment was obtained commercially from Rocky Mountain Instrument Co. For the theoretical estimate of the coupling rate, we used the following parameters: $n = 1.55$, $p_{13} = 0.27$, $\rho = 2648\ \mathrm{kg/m^3}$, $L_{\mathrm{opt}} = 9.13$ mm, $L_{\mathrm{ac}} = 5.19$ mm, $A \simeq \pi \times (61\ \mu\mathrm{m})^2$, $\omega_j = 2\pi \times 193.4$ THz, and $\Omega_m = 2\pi \times 12.65$ GHz (see section S2D).

The Gaussian optical modes, with beam waist $w_{\mathrm{opt}} \simeq 61\ \mu\mathrm{m}$, drive a longitudinal standing-wave phonon mode with Gaussian transverse profile with beam waist $w_{\mathrm{ac}} \simeq 43\ \mu\mathrm{m}$. Therefore, the effective motional mass of the phonon mode in our system $m_{\mathrm{eff}} \approx \pi\rho L_{\mathrm{ac}} w_{\mathrm{ac}}^2/4 = 20\ \mu\mathrm{g}$.

SUPPLEMENTARY MATERIALS

Supplementary material for this article is available at http://advances.sciencemag.org/cgi/content/full/5/4/eaav0582/DC1

Section S1. Asymmetric cavity mode spacing
Section S2. Hamiltonian treatment
Section S3. Optomechanically induced amplification
Section S4. Optomechanically induced transparency
Section S5. Acoustic diffraction loss
Section S6. Thermal fluctuations and phonon lasing
Section S7. Relative scattering rate
Section S8. Phonon counting sensitivity
Fig. S1. Scattering matrix treatment to determine optical mode spectrum.
Fig. S2. Variation of optical FSR with crystal displacement.
Fig. S3. Optical cavity reflection spectrum at cryogenic temperature.
Fig. S4. Normalized coupling rate.
Fig. S5. Cartoons depicting OMIA and OMIT measurements.
Fig. S6. OMIA measurements.
Fig. S7. Acoustic diffraction loss.
Fig. S8. Slope efficiency of the phonon laser.
Fig. S9. Phonon counting in a multiresonant optomechanical system.
Table S1. Optical and acoustic parameters.
References (*44*–*49*)

REFERENCES AND NOTES

1. J. I. Cirac, P. Zoller, Quantum computations with cold trapped ions. *Phys. Rev. Lett.* **74**, 4091–4094 (1995).
2. A. D. O'Connell, M. Hofheinz, M. Ansmann, R. C. Bialczak, M. Lenander, E. Lucero, M. Neeley, D. Sank, H. Wang, M. Weides, J. Wenner, J. M. Martinis, A. N. Cleland, Quantum ground state and single-phonon control of a mechanical resonator. *Nature* **464**, 697–703 (2010).
3. J. Teufel, D. Li, M. Allman, K. Cicak, A. Sirois, J. Whittaker, R. Simmonds, Circuit cavity electromechanics in the strong-coupling regime. *Nature* **471**, 204–208 (2011).
4. Y. Chu, P. Kharel, W. H. Renninger, L. D. Burkhart, L. Frunzio, P. T. Rakich, R. J. Schoelkopf, Quantum acoustics with superconducting qubits. *Science* **358**, 199–202 (2017).
5. T. Stowe, K. Yasumura, T. Kenny, D. Botkin, K. Wago, D. Rugar, Attonewton force detection using ultrathin silicon cantilevers. *Appl. Phys. Lett.* **71**, 288–290 (1997).
6. K. Stannigel, P. Rabl, A. S. Sørensen, P. Zoller, M. D. Lukin, Optomechanical transducers for long-distance quantum communication. *Phys. Rev. Lett.* **105**, 220501 (2010).
7. K. C. Lee, B. J. Sussman, M. R. Sprague, P. Michelberger, K. F. Reim, J. Nunn, N. K. Langford, P. J. Bustard, D. Jaksch, I. A. Walmsley, Macroscopic non-classical states and terahertz quantum processing in room-temperature diamond. *Nat. Photonics* **6**, 41–44 (2012).
8. C. H. Metzger, K. Karrai, Cavity cooling of a microlever. *Nature* **432**, 1002–1005 (2004).
9. A. Schliesser, P. Del'Haye, N. Nooshi, K. Vahala, T. Kippenberg, Radiation pressure cooling of a micromechanical oscillator using dynamical backaction. *Phys. Rev. Lett.* **97**, 243905 (2006).
10. F. Brennecke, S. Ritter, T. Donner, T. Esslinger, Cavity optomechanics with a Bose-Einstein condensate. *Science* **322**, 235–238 (2008).
11. J. D. Thompson, B. M. Zwickl, A. M. Jayich, F. Marquardt, S. M. Girvin, J. G. E. Harris, Strong dispersive coupling of a high-finesse cavity to a micromechanical membrane. *Nature* **452**, 72–75 (2008).
12. M. Eichenfield, J. Chan, R. M. Camacho, K. J. Vahala, O. Painter, Optomechanical crystals. *Nature* **462**, 78–82 (2009).
13. L. Ding, C. Baker, P. Senellart, A. Lemaitre, S. Ducci, G. Leo, I. Favero, High frequency GaAs nano-optomechanical disk resonator. *Phys. Rev. Lett.* **105**, 263903 (2010).
14. G. Bahl, M. Tomes, F. Marquardt, T. Carmon, Observation of spontaneous Brillouin cooling. *Nat. Phys.* **8**, 203–207 (2012).
15. M. Aspelmeyer, T. J. Kippenberg, F. Marquardt, Cavity optomechanics. *Rev. Mod. Phys.* **86**, 1391–1452 (2014).
16. J. Chan, T. M. Alegre, A. H. Safavi-Naeini, J. T. Hill, A. Krause, S. Gröblacher, M. Aspelmeyer, O. Painter, Laser cooling of a nanomechanical oscillator into its quantum ground state. *Nature* **478**, 89–92 (2011).
17. J. D. Cohen, S. M. Meenehan, G. S. MacCabe, S. Gröblacher, A. H. Safavi-Naeini, F. Marsili, M. D. Shaw, O. Painter, Phonon counting and intensity interferometry of a nanomechanical resonator. *Nature* **520**, 522–525 (2015).
18. S. Hong, R. Riedinger, I. Marinković, A. Wallucks, S. G. Hofer, R. A. Norte, M. Aspelmeyer, S. Gröblacher, Hanbury Brown and Twiss interferometry of single phonons from an optomechanical resonator. *Science* **358**, 203–206 (2017).
19. K. C. Lee, M. R. Sprague, B. J. Sussman, J. Nunn, N. K. Langford, X.-M. Jin, T. Champion, P. Michelberger, K. F. Reim, D. England, D. Jaksch, I. A. Walmsley, Entangling macroscopic diamonds at room temperature. *Science* **334**, 1253–1256 (2011).

20. R. Riedinger, A. Wallucks, I. Marinković, C. Löschnauer, M. Aspelmeyer, S. Hong, S. Gröblacher, Remote quantum entanglement between two micromechanical oscillators. *Nature* **556**, 473–477 (2018).
21. C. Ockeloen-Korppi, E. Damskägg, J.-M. Pirkkalainen, M. Asjad, A. Clerk, F. Massel, M. Woolley, M. Sillanpää, Stabilized entanglement of massive mechanical oscillators. *Nature* **556**, 478–482 (2018).
22. O. Arcizet, R. Rivière, A. Schliesser, G. Anetsberger, T. J. Kippenberg, Cryogenic properties of optomechanical silica microcavities. *Phys. Rev. A* **80**, 021803 (2009).
23. S. Galliou, M. Goryachev, R. Bourquin, P. Abbé, J. P. Aubry, M. E. Tobar, Extremely low loss phonon-trapping cryogenic acoustic cavities for future physical experiments. *Sci. Rep.* **3**, 2132 (2013).
24. W. H. Renninger, P. Kharel, R. O. Behunin, P. T. Rakich, Bulk crystalline optomechanics. *Nat. Phys.* **14**, 601–607 (2018).
25. P. Kharel, Y. Chu, M. Power, W. H. Renninger, R. J. Schoelkopf, P. T. Rakich, Ultra-high-*Q* phononic resonators on-chip at cryogenic temperatures. *APL Photonics* **3**, 066101 (2018).
26. M. R. Vanner, M. S. Aspelmeyer, M. Kim, Quantum state orthogonalization and a toolset for quantum optomechanical phonon control. *Phys. Rev. Lett.* **110**, 010504 (2013).
27. A. S. Parkins, H. J. Kimble, Quantum state transfer between motion and light. *J. Opt. B Quantum Semiclass. Opt.* **1**, 496–504 (1999).
28. M. J. Woolley, A. A. Clerk, Two-mode squeezed states in cavity optomechanics via engineering of a single reservoir. *Phys. Rev. A* **89**, 063805 (2014).
29. G. Anetsberger, E. M. Weig, J. P. Kotthaus, T. J. Kippenberg, Cavity optomechanics and cooling nanomechanical oscillators using microresonator enhanced evanescent near-field coupling. *C. R. Phys.* **12**, 800–816 (2011).
30. K. Børkje, S. Girvin, Quantum optomechanics with a high-frequency dilational mode in thin dielectric membranes. *New J. Phys.* **14**, 085016 (2012).
31. M. Mitchell, B. Khanaliloo, D. P. Lake, T. Masuda, J. Hadden, P. E. Barclay, Single-crystal diamond low-dissipation cavity optomechanics. *Optica* **3**, 963–970 (2016).
32. S. Weis, R. Rivière, S. Deléglise, E. Gavartin, O. Arcizet, A. Schliesser, T. J. Kippenberg, Optomechanically induced transparency. *Science* **330**, 1520–1523 (2010).
33. I. S. Grudinin, H. Lee, O. Painter, K. J. Vahala, Phonon laser action in a tunable two-level system. *Phys. Rev. Lett.* **104**, 083901 (2010).
34. P. Kharel, Y. Chu, E. A. Kittlaus, N. T. Otterstrom, S. Gertler, P. T. Rakich, Multimode strong coupling in cavity optomechanics. arXiv:1812.06202 [physics.optics] (14 December 2018).
35. L. S. Meng, J. K. Brasseur, D. K. Neumann, Damage threshold and surface distortion measurement for high-reflectance, low-loss mirrors to 100+ MW/cm^2 cw laser intensity. *Opt. Express* **13**, 10085–10091 (2005).
36. D. Pinnow, T. Rich, Development of a calorimetric method for making precision optical absorption measurements. *Appl. Opt.* **12**, 984–992 (1973).
37. Ö. O. Soykal, R. Ruskov, C. Tahan, Sound-based analogue of cavity quantum electrodynamics in silicon. *Phys. Rev. Lett.* **107**, 235502 (2011).
38. T. Ramos, V. Sudhir, K. Stannigel, P. Zoller, T. J. Kippenberg, Nonlinear quantum optomechanics via individual intrinsic two-level defects. *Phys. Rev. Lett.* **110**, 193602 (2013).
39. J. Bochmann, A. Vainsencher, D. D. Awschalom, A. N. Cleland, Nanomechanical coupling between microwave and optical photons. *Nat. Phys.* **9**, 712–716 (2013).
40. R. W. Andrews, R. W. Peterson, T. P. Purdy, K. Cicak, R. W. Simmonds, C. A. Regal, K. W. Lehnert, Bidirectional and efficient conversion between microwave and optical light. *Nat. Phys.* **10**, 321–326 (2014).
41. K. Jensen, K. Kim, A. Zettl, An atomic-resolution nanomechanical mass sensor. *Nat. Nanotechnol.* **3**, 533–537 (2008).
42. M. E. Tobar, J. G. Hartnett, E. N. Ivanov, D. Cros, P. Blondy, P. Guillon, Cryogenically cooled sapphire-rutile dielectric resonators for ultrahigh-frequency stable oscillators for terrestrial and space applications [atomic frequency standards]. *IEEE Trans. Microw. Theory Tech.* **48**, 1265–1269 (2000).
43. P. Wolf, S. Bize, A. Clairon, A. N. Luiten, G. Santarelli, M. E. Tobar, Tests of Lorentz invariance using a microwave resonator. *Phys. Rev. Lett.* **90**, 060402 (2003).
44. P. T. Rakich, P. Davids, Z. Wang, Tailoring optical forces in waveguides through radiation pressure and electrostrictive forces. *Opt. Express* **18**, 14439–14453 (2010).
45. C. H. Dong, Z. Shen, C. L. Zou, Y. L. Zhang, W. Fu, G. C. Guo, Brillouin-scattering-induced transparency and non-reciprocal light storage. *Nat. Commun.* **6**, 6193 (2015).
46. W. R. Leeb, Losses introduced by tilting intracavity etalons. *Appl. Phys.* **6**, 267–272 (1975).
47. B. L. Green, S. Mottishaw, B. G. Breeze, A. M. Edmonds, U. F. S. D'Haenens-Johansson, M. W. Doherty, S. D. Williams, D. J. Twitchen, M. E. Newton, Neutral silicon-vacancy center in diamond: Spin polarization and lifetimes. *Phys. Rev. Lett.* **119**, 096402 (2017).
48. N. T. Otterstrom, R. O. Behunin, E. A. Kittlaus, Z. Wang, P. T. Rakich, A silicon Brillouin Laser. *Science* **360**, 1113–1116 (2018).
49. K. J. Vahala, Back-action limit of linewidth in an optomechanical oscillator. *Phys. Rev. A* **78**, 023832 (2008).

Acknowledgments: We thank Y. Chu, V. Jain, S. Gertler, T. Yoon, C. Brown, Y. Zhou, and Y. Luo for helpful discussions and feedback. **Funding:** We acknowledge funding support from ONR YIP (N00014-17-1-2514), NSF MRSEC (DMR-1119826), AFOSR (FA9550-09-1-0484 and FA9550-15-1-0270), ONR MURI on Quantum Optomechanics (award no. N00014-15-1-2761), and the Packard Fellowship for Science and Engineering. N.T.O. acknowledges support from the NSF Graduate Research Fellowship under grant no. DGE1122492. **Author contributions:** P.K., G.I.H., and E.A.K. performed the experiments, and P.K. analyzed the data with input from J.G.E.H. and P.T.R. P.K. developed the analytical theory with guidance from G.I.H., J.G.E.H., and P.T.R. W.H.R. contributed to the models of photon-phonon coupling, and N.T.O. aided in the development of experimental techniques. All authors participated in the writing of this manuscript. **Competing interests:** The authors declare that they have no competing interests. **Data and materials availability:** All data needed to evaluate the conclusions in the paper are present in the paper and/or the Supplementary Materials. Additional data related to this paper may be requested from the authors.

Submitted 9 August 2018
Accepted 13 February 2019
Published 5 April 2019
10.1126/sciadv.aav0582

Citation: P. Kharel, G. I. Harris, E. A. Kittlaus, W. H. Renninger, N. T. Otterstrom, J. G. E. Harris, P. T. Rakich, High-frequency cavity optomechanics using bulk acoustic phonons. *Sci. Adv.* **5**, eaav0582 (2019).

Science Advances

High-frequency cavity optomechanics using bulk acoustic phonons

Prashanta Kharel, Glen I. Harris, Eric A. Kittlaus, William H. Renninger, Nils T. Otterstrom, Jack G. E. Harris and Peter T. Rakich

Sci Adv **5** (4), eaav0582.
DOI: 10.1126/sciadv.aav0582

Science Advances (ISSN 2375-2548) is published by the American Association for the Advancement of Science, 1200 New York Avenue NW, Washington, DC 20005. The title *Science Advances* is a registered trademark of AAAS.

Science Advances
AAAS

advances.sciencemag.org/cgi/content/full/5/4/eaav0582/DC1

Supplementary Materials for

High-frequency cavity optomechanics using bulk acoustic phonons

Prashanta Kharel*, Glen I. Harris, Eric A. Kittlaus, William H. Renninger, Nils T. Otterstrom,
Jack G. E. Harris, Peter T. Rakich*

*Corresponding author. Email: prashanta.kharel@yale.edu (P.K.); peter.rakich@yale.edu (P.T.R.)

Published 5 April 2019, *Sci. Adv.* **5**, eaav0582 (2019)
DOI: 10.1126/sciadv.aav0582

This PDF file includes:

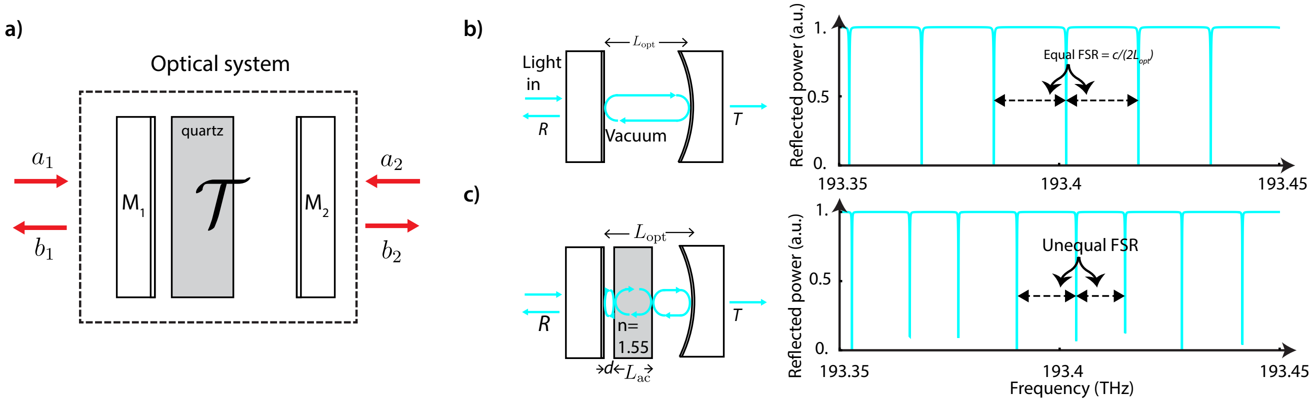

Fig. S1. Scattering matrix treatment to determine optical mode spectrum. **a** A cartoon of our optical system, which consists of two optical mirrors with a quartz crystal placed in between them. A transfer matrix ($\mathcal{T}$) relates the incoming and outgoing optical fields in our system. **b**, For an optical cavity in vacuum, the standing wave cavity modes are spaced equally by the optical free spectral range (FSR) given by $c/2L_{\rm opt}$. **c**, The mode spectrum of an optical cavity can vary quite dramatically when a medium with refractive index n is placed in between the mirrors. As expected the frequency spacing between the optical modes decreases because of increase in the optical path length. In addition, there is a variation in the optical free spectral range (i.e., change in the spacing between adjacent optical modes) as a function of frequency. Surprisingly, a large variation in FSR ($\sim 21\%$) occurs even though the reflectivity of the quartz-vacuum interface is rather small ($\sim 4\%$).

Section S1. Asymmetric cavity mode spacing

In this section, we use scattering/transmission matrix approach to calculate the mode spectrum of an optical cavity consisting of a bulk crystal placed in between two mirrors (see fig. S1a). Unlike equally spaced standing-wave longitudinal modes of an optical cavity in vacuum, we show that our optical system supports a rich mode spectrum with mode spacing that vary dramatically as a function of both the optical mode number and the crystal position. Our one dimensional model consists of a Fabry-Pérot optical cavity having power reflectivities of R_1 and R_2 and transmission of T_1 and T_2. A dielectric material of index n is placed in between the two mirrors. We assume the mirrors are lossless so that $R_i + T_i = 1$, where $i = 1, 2$. The power reflectivity at each crystal face, R_0, is given by $(1-n)^2/(1+n)^2$. For simplicity, we assume plane wave optical fields and focus on the cavity's reflection and transmission spectrum.

We define the plane wave optical fields propagating along positive direction as $E = \mathrm{Re}\{ae^{i(kz-\omega t)}\}$. The phase ϕ acquired by the plane wave after propagating a distance z in a medium with refractive index n is given by $\phi = kz = n\omega z/c$, where c is the speed of light in vacuum. A transmission matrix ($\mathcal{T}$) relates the input field amplitudes a_1, a_2 and output field amplitudes b_1, b_2 (see fig. S1a) in our system as follows

$$\begin{bmatrix} b_1 \\ a_1 \end{bmatrix} = \mathcal{T} \begin{bmatrix} b_2 \\ a_2 \end{bmatrix} \tag{S1}$$

The transmission matrices for a lossless mirror and for propagation in space are given by

$$\mathcal{T}_{\rm mirror} = \frac{-i}{t} \begin{bmatrix} -1 & r \\ -r & 1 \end{bmatrix} \text{ and } \mathcal{T}_{\rm prop} = \begin{bmatrix} e^{i\phi} & 0 \\ 0 & e^{-i\phi} \end{bmatrix} \tag{S2}$$

The total transmission matrix for our optical system consisting of the bulk crystal inside the Fabry-Pérot optical cavity is then given by

$$\begin{aligned} \mathcal{T} &= \mathcal{T}_{mirror1} \cdot \mathcal{T}_{propVacuum} \cdot \mathcal{T}_{mirrorQuartz} \cdot \mathcal{T}_{propQuartz} \cdot \mathcal{T}_{mirrorQuartz} \cdot \mathcal{T}_{propVacuum} \cdot \mathcal{T}_{mirror2} \\ &= \frac{-i}{t_1} \begin{bmatrix} -1 & r_1 \\ -r_1 & 1 \end{bmatrix} \cdot \begin{bmatrix} e^{i\phi_1} & 0 \\ 0 & e^{-i\phi_1} \end{bmatrix} \cdot \frac{-i}{t_0} \begin{bmatrix} -1 & r_0 \\ -r_0 & 1 \end{bmatrix} \cdot \begin{bmatrix} e^{i\phi_2} & 0 \\ 0 & e^{-i\phi_2} \end{bmatrix} \cdot \frac{-i}{t_0} \begin{bmatrix} -1 & -r_0 \\ r_0 & 1 \end{bmatrix} \\ &\cdot \begin{bmatrix} e^{i\phi_3} & 0 \\ 0 & e^{-i\phi_3} \end{bmatrix} \cdot \frac{-i}{t_2} \begin{bmatrix} -1 & r_2 \\ -r_2 & 1 \end{bmatrix} \end{aligned} \tag{S3}$$

Here $r_1 = \sqrt{R_1}, r_2 = \sqrt{R_2}, r_0 = (1-n)/(1+n), \phi_1 = \omega t/c, \phi_2 = n\omega L_{\rm ac}/c$, and $\phi_3 = \omega(L_{\rm opt} - L_{\rm ac} - t)/c$. The optical power reflected (P_r) from and transmitted (P_t) through our optical system can then be calculated from the total transmission matrix as follows

$$P_r = \left|\frac{\mathcal{T}_{12}}{\mathcal{T}_{22}}\right|^2 \text{ and } P_t = \left|\frac{1}{\mathcal{T}_{22}}\right|^2 \tag{S4}$$

The analytical expressions for P_r and P_t can be derived in a straightforward way from eqn. (S3); we chose to not show them here because they are quite cumbersome to display.

Next, we use the analytical expression for P_r along with the known geometrical parameters (d= 0.15 mm, L_{ac} = 5.19 mm, L_{opt}= 9.13 mm, and n= 1.55) and mirror reflectivities ($R_1 = R_2 = 0.98$) to explore the reflection spectrum of our optical cavity (see fig. S1b-c). We compare the cavity mode spectrum with and without the quartz crystal inside the optical cavity near experimentally relevant wavelength (1550 nm or $\omega/2\pi \sim$ 194 THz). Without the crystal inside the optical cavity, this analytical calculation reveals equally spaced cavity modes, which are separated by the well known optical free spectral range given by $c/(2L_{\text{opt}})$. However, when the quartz crystal is placed inside an optical cavity, we notice that the average spacing between the optical modes gets narrower; this result makes sense as the optical path length is longer when the crystal is placed inside the cavity. Moreover, we observe a variation in free spectral range (i.e., change in the spacing between adjacent optical modes) as a function of cavity frequency.

We explored this variation in FSR analytically by changing the parameter d, corresponding to the position of the crystal inside the cavity (see fig S2a). We observed periodic variations in cavity mode frequencies for each mode number j (see fig. S2b) as a function of the crystal displacement (Δd). This variation in cavity frequency was $\lambda/2$ periodic, where λ is the wavelength of the light; this is a result of the crystal surfaces passing through the nodes and anti-nodes of the standing wave optical cavity modes. Notice that the amount of frequency variation is different for each cavity mode. Consequently, the free-spectral range changes both as a function of the cavity mode number (j) and the crystal position. Therefore, it is relatively easy to tune the FSR to match the Brillouin frequency in this system.

From theory, we expect a maximum FSR variation as large as 2.94 GHz between 1548 nm and 1552 nm (see fig. S2c). Furthermore, the difference in FSR between adjacent optical modes (χ_j = FSR$_{j+1}$-FSR$_j$) can be as large as 2.47 GHz; the parameter χ_j is important because it quantifies the degree of asymmetry between the Stokes and the anti-Stokes scattering processes. Additionally, since the FSR variation is periodic as a function of cavity frequency, it is possible to find several pairs of cavity modes having FSRs that equal Brillouin frequency.

Next, we compare experimental measurement of the cavity mode spacing with the analytical calculations discussed above. The reflection spectrum of the cavity was measured at cryogenic temperature ($\sim$ 8 K) by sweeping the laser wavelength between 1548 nm and 1552 nm and recording the back-reflected power (see fig. S3). After identifying the resonant frequencies, $\omega_j/2\pi$, we calculate the cavity mode spacing by simply taking the difference of two adjacent mode frequencies (i.e., FSR$_j$= $(\omega_{j+1}-\omega_j)/2\pi$). This analysis revealed periodic variation (see fig. S3b) in cavity mode spacing, which was similar to the one predicted from theoretical calculation as seen in fig. S2c. However, because of the uncertainties in the geometrical parameters (such as a exact crystal position t) as we cool our system to cryogenic temperatures. Therefore, we took the exact crystal location as a free parameter. For t = 152.52 μm, we see a good agreement between the experimentally determined cavity mode spacing (black dots) and the theoretically calculated values (green dots) in fig. S3c. With the quartz crystal inside the optical cavity, the maximum FSR variation of 2.6 GHz obtained experimentally agrees well with the predicted value of 2.94 GHz.

Section S2. Hamiltonian treatment

In this section, we derive the total Hamiltonian for our optomechanical system. We first derive the Hamiltonian for the optical and the acoustic fields and eventually add an interaction term that characterizes the acousto-optic interaction.

A. Hamiltonian for the electromagnetic fields

We consider the case of an electromagnetic field having a single single polarization ($\hat{x}-$direction) that is subjected to the boundary conditions defined by the two mirrors. For simplicity, we assume that the electric field vanishes at the location of the left mirror ($z = 0$) and the right mirror ($z = L_{\text{opt}}$). Hence, when we expand the electric field into the normal modes (standing waves) of the optical cavity

$$E_x(z,t) = \sum_j E_j \sin(k_j z)(\hat{a}_j(t) + \hat{a}_j^\dagger(t)) \tag{S5}$$

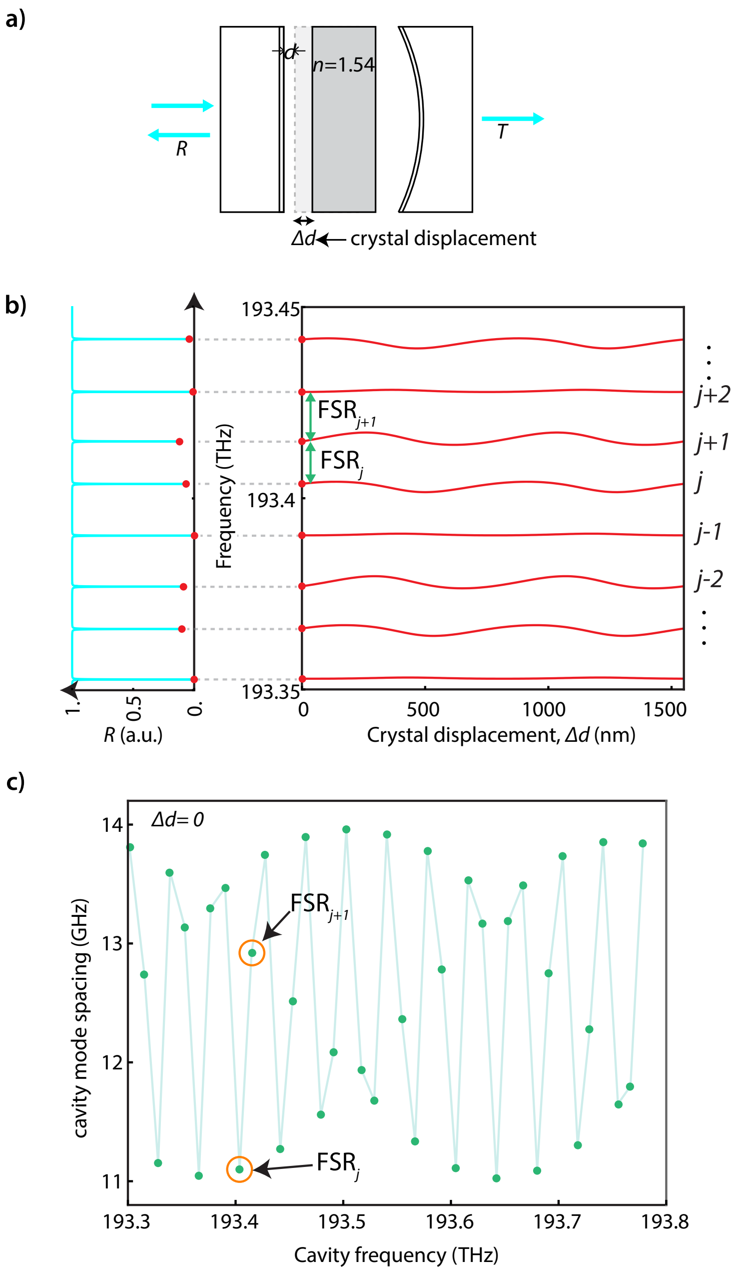

Fig S2.Variation of optical FSR with crystal displacement. **a**, A schematic showing how the crystal is displaced from its original location d to $d + \Delta d$. **b**, Plot of the resonant cavity modes, labeled with the longitudinal mode number j, reveals periodic variation in the mode frequency as a function of the cavity displacement (Δd). This periodicity is equal to half the wavelength of light ($\sim$1550 nm), corresponding to the crystal moving through the nodes and the anti-nodes of the standing wave optical cavity modes. Although periodic, the extent of variation in the cavity frequency is different for each mode; as a result, we obtain a non-trivial variation in the cavity FSR as a function of optical mode number j seen in **c**.

where $\hat{a}_j$ is the normal mode amplitude, $k_j = \omega_j/c$, with j = 1, 2, 3, ..., and the zero-point amplitude of the electric field is

$$E_j = \sqrt{\frac{\hbar\omega_j}{\epsilon_0 \epsilon_r^{\text{eff}} A_{\text{opt}} L_{\text{opt}}}} \tag{S6}$$

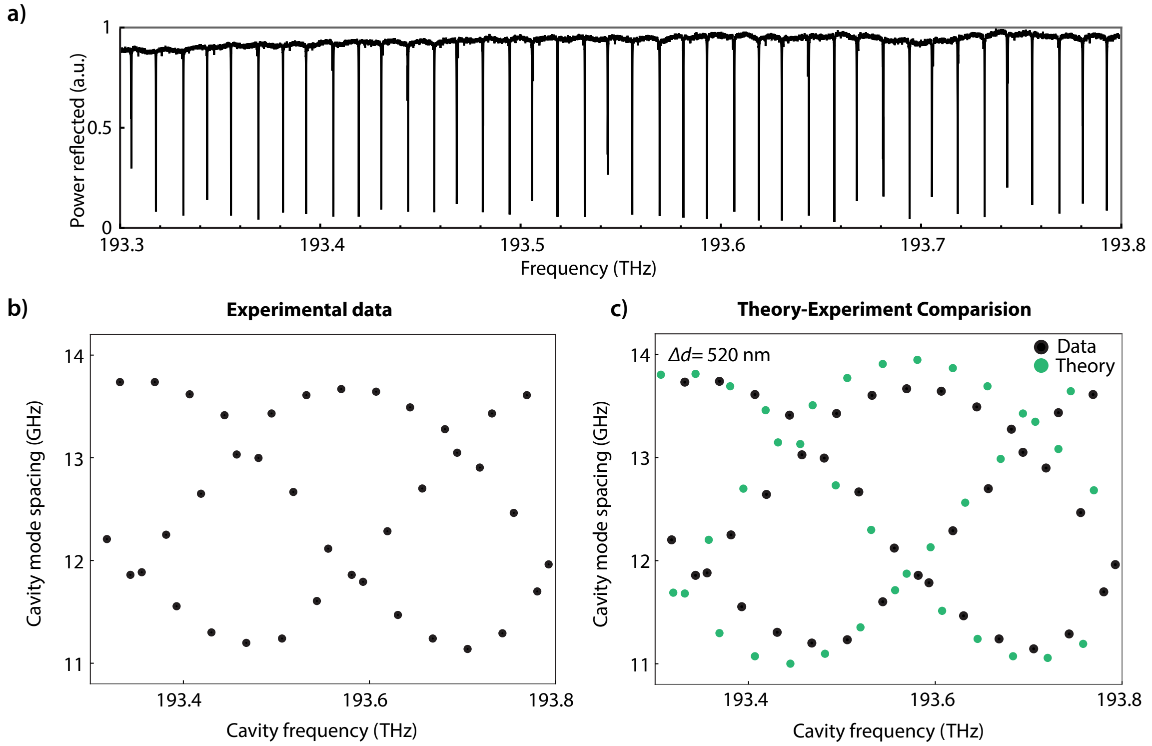

Fig. S3.Optical cavity reflection spectrum at cryogenic temperature. **a**, Measurement from 1548 nm to 1552 nm (or 193.3 GHz to 193.8 GHz) (at $\sim$ 8 K) revealed narrow optical resonances corresponding to longitudinal cavity modes. Some modes have larger dip depths than others as expected from theoretical calculations. **b**, We see periodic variation in FSR as a function of the cavity frequency (or mode number j). This variation is similar to what was predicted from theoretical analysis. **c**, To compare theory with experiments, we first change the crystal displacement (Δd); we take this crystal displacement as a fit parameter as the relative spacing between the crystal and the mirror can change during the cryogenic refrigeration process. When we choose $\Delta d = 520$ nm, we see that the theoretically obtained mode spacing matches well with the experimentally obtained data. The maximum FSR variation of 2.6 GHz observed experimentally is close to the theoretically predicted value of 2.94 GHz.

where ω_j is the frequency of the normal mode, ϵ_r^{eff} is the effective relative permittivity of the optical cavity, A_{opt} is the effective transverse area of the optical mode, and L_{opt} is the optical cavity length. The zero-point fluctuation of the electric field was obtained knowing that the total electromagnetic energy per mode for the ground state is $\hbar\omega_j/2$. Starting with the Hamiltonian for the electromagnetic fields

$$H^{\text{opt}} = \frac{1}{2}\int_V dV \; (\epsilon E^2 + \mu_o H^2) \tag{S7}$$

and substituting the normal mode expansions for the electromagnetic fields, we obtain the quantized version of the electromagnetic Hamiltonian given by

$$\hat{H}^{\text{opt}} = \sum_j \hbar\omega_j \left(\hat{a}_j^\dagger \hat{a}_j + \frac{1}{2}\right) \tag{S8}$$

Note that the mode amplitude operators satisfy the commutation relations $[\hat{a}_j, \hat{a}_{j'}^\dagger] = \delta_{j,j'}$ and $[\hat{a}_j, \hat{a}_j'] = [\hat{a}_j^\dagger, \hat{a}_{j'}^\dagger] = 0$.

B. Hamiltonian for the acoustic fields

For the quantization of acoustic fields, we consider a longitudinally polarized ($\hat{z}$-direction) acoustic field subject to free boundary conditions at the surfaces of the crystal, which forms an acoustic Fabry-Pérot cavity. As a starting point, we assume that the separation between the mirror and the crystal face (d) is vanishingly small (i.e., the crystal is flush with the mirror). We expand the acoustic displacement field into the normal modes (standing waves) of the Fabry-Pérot acoustic cavity

$$u_z(z,t) = \sum_m U_m \cos(q_m z)(\hat{b}_m(t) + \hat{b}_m^\dagger(t)) \tag{S9}$$

where $\hat{b}_m$ is the normal mode amplitude, $q_m = m\pi/L_{ac}$, with $m = 1, 2, 3, \ldots$, and the zero-point amplitude of the acoustic displacement field

$$U_m = \sqrt{\frac{\hbar}{\rho A_{\text{ac}} L_{\text{ac}} \Omega_m}} \tag{S10}$$

Here Ω_m is the frequency of the acoustic mode, ρ is the density of the medium, A_{ac} is the effective transverse area of the acoustic mode, and L_{ac} is the thickness of the acoustic Fabry-Pérot cavity. The zero-point fluctuation of the acoustic field was calculated knowing that the total acoustic energy (kinetic plus potential) per mode for the ground state is $\hbar\Omega_m/2$. We start with the acoustic Hamiltonian

$$H^{\text{ph}} = \frac{1}{2}\int_V dV \,\left(\rho\dot{u}^2 + C\left(\frac{\partial u}{\partial z}\right)^2\right) \tag{S11}$$

where $C = v_{\text{ac}}^2\rho$ is the elastic coefficient and substitute the normal mode expansion to obtain the quantized version of the acoustic field

$$\hat{H}^{\text{ph}} = \sum_m \hbar\Omega_m \left(\hat{b}_m^\dagger \hat{b}_m + \frac{1}{2}\right) \tag{S12}$$

Note that the mode amplitude operators satisfy the commutation relations $[\hat{b}_m, \hat{b}_{m'}^\dagger] = \delta_{m,m'}$ and $[\hat{b}_m, \hat{b}_m'] = [\hat{b}_m^\dagger, \hat{b}_{m'}^\dagger] = 0$.

C. Interaction Hamiltonian

We now consider the interaction Hamiltonian for the optomechanical coupling (see Ref. [43]), which is given by

$$H^{\text{int}} = \frac{1}{2}\int_V dV \,\epsilon_0\epsilon_r^2 E^2 p_{13}\frac{\partial u}{\partial z}, \tag{S13}$$

where p_{13} is the relevant photoelastic constant. Substituting the normal mode expansions for the electric field and the acoustic displacement field from eqn. (S5) and eqn. (S9) into this interaction Hamiltonian and using the rotating wave approximation, we obtain

$$\hat{H}^{\text{int}} = -\sum_{j,j',m}\int dV \,\epsilon_0\epsilon_r^2 p_{13} q_m U_m E_j E_{j'} \,\sin(k_j z)\sin(k_{j'} z)\sin(q_m z)\,(\hat{a}_j^\dagger \hat{a}_{j'} \hat{b}_m + \hat{a}_j \hat{a}_{j'}^\dagger \hat{b}_m^\dagger). \tag{S14}$$

The term $\hat{a}_j^\dagger \hat{a}_{j'} \hat{b}_m$ in the interaction Hamiltonian represents the annihilation of an optical mode at frequency $\omega_{j'}$ and a phonon mode at frequency Ω_m to create a photon mode at higher frequency $\omega_j = \omega_{j'} + \Omega_m$ (also called the anti-Stokes process). The other term $\hat{a}_j \hat{a}_{j'}^\dagger \hat{b}_m^\dagger$ represents the conjugate process, whereby a photon at lower frequency $\omega_{j'}$ and a phonon at frequency Ω_m are created from the annihilation of photon at ω_j (Stokes process).

Now, if we consider two adjacent standing wave optical modes such that $\omega_{j+1} - \omega_j = \Omega_m$, the interaction Hamiltonian for the coupling to the m-th phonon mode is given by

$$\hat{H}_m^{\text{int}} = -\hbar g_0^m (\hat{a}_{j+1}^\dagger \hat{a}_j \hat{b}_m + \text{H.c.}) \tag{S15}$$

where the single-photon coupling rate for this multi-mode optomechanical system is given by

$$g_0^m = \frac{1}{\hbar}\int dV \,\epsilon_0\epsilon_r^2 p_{13} q_m U_m E_{j+1} E_j \,\sin(k_{j+1} z)\sin(k_j z)\sin(q_m z) \tag{S16}$$

Note that, up to this point, we have assumed that the crystal face is flush with the mirror 1, meaning $d = 0$.

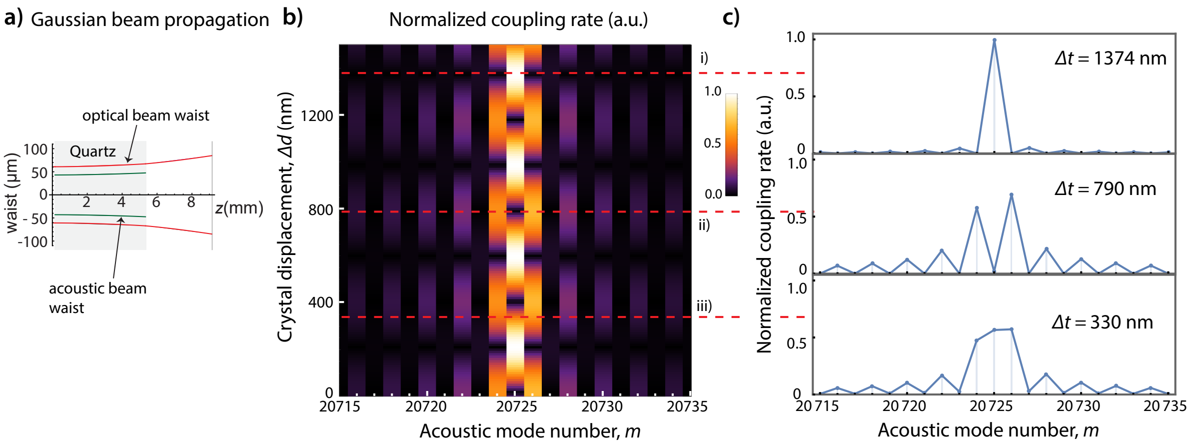

Fig. S4. Normalized coupling rate. a, We use Gaussian beam propagation to determine the beam waist of the fundamental longitudinal optical mode inside our optical cavity. The driven acoustic wave inside the crystal also has a Gaussian transverse mode profile determined by the optical forcing function, which is proportional to the product of pump and Stokes optical field. **b**, We observe that appreciable optomechanical coupling occurs over a small set of phonon modes (indexed by longitudinal mode number m) near the Brillouin frequency. The optomechanical coupling to a single-mode (say m = 20725) is periodic and can go to zero at certain crystal positions. Nevertheless, for an arbitrary crystal displacement, we still have an appreciable coupling at least one phonon mode. **c**, Line cuts in the 2-Dimensional density plot of the normalized coupling rate shows that tailorable coupling to one (inset **i**), two (inset **ii**) or three phonon modes (inset **iii**) can be achieved by changing the crystal displacement.

D. Single-photon coupling rate

We use the definition of the coupling rate given in eqn. (S16) along with the zero-point amplitudes of the electric and the acoustic fields (eqn. (S6) and eqn. (S10)) to calculate the single photon coupling rate

$$g_0^m = \frac{1}{\hbar}\int dV\ \epsilon_0\epsilon_r^2 p_{13} q_m U_m E_{j+1} E_j\ \sin(k_{j+1}z)\ \sin(k_j z)\ \sin(q_m z) \tag{S17}$$

This definition of coupling rate, when we account for the finite separation (d) between the mirror and the crystal, becomes

$$g_0^m = A\epsilon_0\epsilon_r^2 p_{13} q_m \sqrt{\frac{\hbar}{\rho A L_{\text{ac}}\Omega_m}}\,\frac{\sqrt{\omega_j\omega_{j+1}}}{\epsilon_0\epsilon_r^{\text{eff}} A L_{\text{opt}}}\times \int_d^{d+L_{\text{ac}}} dz\ \sin\left(k'_{j+1}\left(z-d+\frac{d}{n}\right)\right)\sin\left(k'_j\left(z-d+\frac{d}{n}\right)\right)\sin\left(q_m(z-d)\right) \tag{S18}$$

where d is a variable crystal position, and we are considering only the optical fields living inside the crystal for the acousto-optic overlap in z, and for simplicity we have assumed $A_{\text{ac}} = A_{\text{opt}} \equiv A$. Here, $k'_j = nk_j$ denotes the wavevector of the optical modes inside the crystal. The phase factors for the sine functions come from the appropriate boundary conditions on the electric and acoustic fields at the crystal and mirror surfaces.

Using a trigonometric identity

$$\sin(\text{A})\cdot\sin(\text{B})\cdot\sin(\text{C}) = 1/4(\text{-sin(A-B-C)+sin(A+B-C)+sin(A-B+C)-sin(A+B+C)}) \tag{S19}$$

we see that non-zero spatial overlap and, hence, a non-zero coupling rate occurs when the phase matching requirement ($q_m = k'_{j+1} + k'_j$) is satisfied. Note that this equation also shows that one can change the coupling rate by changing the crystal position. For example, as the crystal position is changed along the z-direction the nodes of the strain profile could line up with the anti-nodes of the optical beat tone (or the forcing function) resulting in zero optomechanical coupling. For maximum coupling rate to a single acoustic mode, the crystal position (or the optical wavevector) has to be such that the nodes (anti-nodes) of the strain profile line up with the nodes (anti-nodes) of the optical beat tone. In this case, the maximum coupling rate can be calculated from eqn. (S17) and is given by

$$\tilde{g}_0 \approx \frac{\omega_j^2 n^5 p_{13}}{2cn_{\text{eff}}^2}\sqrt{\frac{\hbar}{\rho A L_{\text{ac}}\Omega_m}}\,\frac{L_{\text{ac}}}{L_{\text{opt}}} \tag{S20}$$

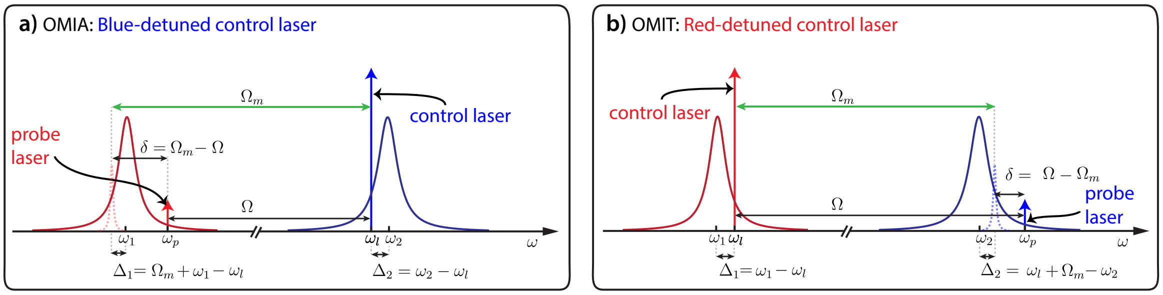

Fig. S5.Cartoons depicting OMIA and OMIT measurements. a, A strong blue-detuned control laser is resonant with the higher frequency optical mode while a weak probe is swept near the lower frequency optical mode. **b**, A strong red-detuned control laser is resonant with the low frequency optical mode while a weak probe is swept near the higher frequency optical mode.

where n_{eff} is the effective refractive index of the optical mode, and we assumed $\omega_{j+1} \simeq \omega_j$, so that $q_m = k'_{j+1} + k'_j \approx 2n\omega_j/c$. We note that the phase matching ($q_m = k'_{j+1} + k'_j$) and energy conservation ($\omega_{j+1} - \omega_j = \Omega_m$) is satisfied for modes near $\Omega_m \approx 2\omega_j n v_a/c$, where v_a is the velocity of sound inside the medium. Note that the simplified derivation presented above gives us insights into the dependence of g_0 on various material and geometric parameters. However, to calculate the coupling rate within our actual system, we perform acousto-optical overlap intergal in Eq. (S18), taking into account the variation (~ 30 %)in traverse mode area of the Gaussian optical and acoustic modes inside the cavity (See fig. S4a).

For instance, for two Gaussian optical modes near 1551.0335 nm (i.e., $\omega_j = 2\pi \times 193.4$ THz) separated by the phonon frequency of $\Omega_m/2\pi = 12.645$ GHz, we calculate a maximum coupling rate $g_0^m/2\pi \simeq 24$ Hz in our system. Note that we used the following experimentally relevant geometric and material parameters for the calculation of g_m^0: $p_{13} = 0.27,\ n = 1.55,\ \rho = 2648\ \text{kg/m}^3,\ v_a = 6327\ \text{m/s},\ L_{\text{ac}} = 5.19\ \text{mm},$ and $L_{\text{opt}} = 9.13$ mm.

Next, we explore the coupling rate variation as a function of the crystal position for several longitudinal acoustic modes near the Brillouin frequency. We define a normalized coupling rate as $|g_0^m|/\tilde{g}_0$, and calculate optomechanical coupling to phonon modes the Brillouin frequency; the Brillouin frequency of 12.645 GHz corresponds to a very large mode number (m= 20725). It is important to note that the precise value of the mode number is not well known due to the uncertainties in the geometrical parameters and elastic constants at cryogenic temperatures. Our aim here is to simply compare optomechanical coupling to the longitudinal modes near the Brillouin frequency. A density plot in fig. S4b reveals that appreciable optomechanical coupling occurs to a few modes near the Brillouin frequency. This occurs because of the finite spatial integral in eqn. (S17); as a result of the finite length of the crystal, there is an uncertainty in the acoustic wave-vector which relaxes the phase matching condition and grants optomechanical coupling to more than one phonon modes (see Ref. [24]). The bandwidth of coupling ($\Delta\nu_B = 1.76 v_a/2L_{\text{ac}}$) is ~ 1.1 MHz in our system.

The coupling to an individual phonon mode (say m= 20725) is periodic in the crystal displacement (see fig. S4b) and it can be zero at certain crystal positions (see fig. S4c.ii). Nevertheless, appreciable optomechanical coupling (normalized coupling rate > 0.5) occurs for at least one phonon mode irrespective of the crystal displacement. Therefore, as long as the linewidth of the optical mode ($\kappa/2\pi$) is greater than the coupling bandwidth ($\Delta\nu_B$), we observe appreciable optomechanical coupling to at least one phonon mode irrespective of the crystal position. For a given pair of optical modes, changing the crystal position using a piezo-actuator should enable controllable optomechanical coupling to one or more phonon modes in our system (see fig. S4c.i-iii). Alternatively, coupling to one or more phonon modes can be engineered by changing the wavevector of the optical fields by moving to a different pair of optical resonances (with frequency difference matching the Brillouin frequency). We can use eqn. (S17) to see that the relative coupling rate to phonon modes near Brillouin frequency changes as we change the wave-vector (or the frequency) of the optical modes modes. This approach avoids the experimental complexity of adding a piezo-actuator in our optomechanical system.

Section S3. Optomechanically induced amplification (OMIA)

In this section, we follow the approach outlined in Ref. [44] to derive the intra-cavity optical spectrum during OMIA measurements. The optomechanical Hamiltonian accounting for the external drive fields (i.e., the control laser

Table S1. Optical and acoustic parameters. We choose a pair of optical modes separated by the Brillouin frequency for OMIA/OMIT measurements. The loss rate of each cavity mode was obtained separately from the OMIA/OMIT measurements by sweeping the tunable laser source through the optical resonances and measuring the reflection spectrum.

Parameters	values
ω_2	$2\pi\times$ 193.419 THz
Ω_m	$2\pi\times$ 12.645 GHz
κ_1	$2\pi\times$ 71 MHz
κ_2	$2\pi\times$ 81 MHz
κ_1^{ext}	$\kappa_1/2$
κ_2^{ext}	$\kappa_2/2$

and the probe laser) is given by

$$\begin{aligned}H &= \hbar\omega_1 a_1^\dagger \hat{a}_1 + \hbar\omega_2 a_2^\dagger a_2 + \hbar\Omega_m b_m^\dagger b_m - \hbar g_0^m (a_2^\dagger a_1 b_m + b_m^\dagger a_1^\dagger a_2) \\ &\quad + i\hbar\sqrt{\kappa_1^{\text{ext}}}\alpha_p (a_1^\dagger e^{-i\omega_p t} - a_1 e^{i\omega_p t}) + i\hbar\sqrt{\kappa_2^{\text{ext}}}\alpha_l (a_2^\dagger e^{-i\omega_l t} - a_2 e^{i\omega_l t})\end{aligned} \tag{S21}$$

We normalize the optical power launched into the cavity such that $P_{in} = \hbar\omega \langle \alpha^\dagger \alpha \rangle$. We assume a strong control laser and a weak probe; within the undepleted pump approximation, the dynamics of the mode at frequency ω_2 is not influenced by the optomechanical coupling and it can be described by the following equation of motion derived from the Hamiltonian in eqn. (S21)

$$\dot{a}_2(t) = \left(-i\omega_2 - \frac{\kappa_2}{2}\right) a_2 + \sqrt{\kappa_2^{\text{ext}}}\alpha_l e^{-i\omega_l t} \tag{S22}$$

where $\kappa_2 = 2\kappa_2^{\text{ext}} + \kappa_2^0$, κ_2^{ext} is the loss rate at each cavity mirror and k_2^0 is the loss rate inside the cavity. We assume negligible internal losses in our system ($k_2^0 \ll 2\kappa_2^{\text{ext}}$). From eqn. (S22), we obtain the following steady state solution for mode a_2

$$\langle a_2 \rangle = \sqrt{N_2} e^{-i\omega_l t} = \left| \frac{\sqrt{\kappa_2^{\text{ext}}}\alpha_l}{i\Delta_2 + \kappa_2/2} \right| e^{-i\omega_l t} \tag{S23}$$

where N_2 is the control laser driven intra-cavity photon number for mode a_2, and $\Delta_2 = \omega_2 - \omega_l$ (see Supplementary Note fig. S5). Once we know the intra-cavity photon number for mode $a_{\,2}$ we use input-output formalism for a symmetric Fabry-Pérot cavity to obtain the transmitted light field

$$a_{2,\text{out}} = \sqrt{\kappa_2^{\text{ext}}} a_2 \tag{S24}$$

In the undepleted pump regime, we substitute $\langle a_2 \rangle$ from eqn. (S23) into the Hamiltonian of eqn. (S38) to derive the following linearized Hamiltonian for the interaction between the optical mode a_1 and the phonon mode b_m

$$H = \hbar\omega_1 a_1^\dagger a_1 + \hbar\Omega_m b_m^\dagger b_m - \hbar g_0^m \sqrt{N_2}(a_1 b_m e^{i\omega_l t} + a_1^\dagger b_m^\dagger e^{-i\omega_l t}) + i\hbar\sqrt{\kappa_1^{\text{ext}}}\alpha_p (a_1^\dagger e^{-i\omega_p t} - a_1 e^{i\omega_p t}) \tag{S25}$$

From this Hamiltonian, by rotating in the frame of $H_0 = \hbar(\omega_l - \omega_p) b_m^\dagger b_m + \hbar\omega_p a_1^\dagger a_1$ (i.e. $a_1(t) \to a_1(t) e^{-i\omega_p t}$ and $b_m(t) \to b_m(t) e^{-i(\omega_l - \omega_p)t}$), we obtain an effective Hamiltonian

$$H_{\text{eff}} = \hbar\delta b_m^\dagger b_m - \hbar(\delta - \Delta_1) a_1^\dagger a_1 - \hbar g_m (a_1 b_m + a_1^\dagger b_m^\dagger) + i\hbar\sqrt{\kappa_1^{\text{ext}}}\alpha_p (a_1^\dagger - a_1) \tag{S26}$$

where $\delta = \Omega_m - \Omega = \Omega_m - \omega_l + \omega_p$, and $\Delta_1 = \Omega_m + \omega_1 - \omega_l$, and the cavity field-enhanced coupling rate $g_m = g_0^m \sqrt{N_2}$. The Heisenberg equations of motions derived from this Hamiltonian

$$\dot{a}_1(t) = \left(i(\delta - \Delta_1) - \frac{\kappa_1}{2}\right) a_1 + i g_m b_m^\dagger + \sqrt{\kappa_1^{\text{ext}}}\alpha_p \tag{S27}$$

$$\dot{b}_m(t) = \left(-i\delta - \frac{\Gamma_m}{2}\right) b_m + i g_m a_1^\dagger \tag{S28}$$

can be used to derive steady state values for the phonon and photon numbers

$$b_m = \frac{ig_m}{\left(i\delta + \frac{\Gamma_m}{2}\right)} a_1^\dagger \tag{S29}$$

$$a_1 = \frac{-\sqrt{\kappa_1^{\text{ext}}}\alpha_p}{i(\delta - \Delta_1) - \frac{\kappa_1}{2} + \frac{g_m^2}{-i\delta + \Gamma_m/2}} \tag{S30}$$

As before, we can use the input-output formalism to obtain the transmitted probe light given by

$$a_{1,\text{out}} = \sqrt{\kappa_1^{\text{ext}}} a_1 = -\frac{\kappa_1^{\text{ext}}\alpha_p}{i(\delta - \Delta_1) - \frac{\kappa_1}{2} + \frac{g_m^2}{-i\delta + \Gamma_m/2}} \tag{S31}$$

In experiments, we use heterodyne detection of the transmitted probe light to measure the intra-cavity photon number. The power spectrum of this heterodyne signal at the detector is given by

$$P_d(\delta) \propto \langle a_{1,\text{out}}^\dagger a_{1,\text{out}} \rangle = \left| \frac{\kappa_1^{\text{ext}}}{i(\delta - \Delta_1) - \frac{\kappa_1}{2} + \frac{g_m^2}{-i\delta + \Gamma_m/2}} \right|^2 \tag{S32}$$

If we assume that the frequency difference between the optical modes is exactly equal to the Brillouin frequency ($\omega_2 - \omega_1 = \Omega_m$) and the control laser is directly on resonance with the optical cavity mode a_2 ($\Delta_2 = \Delta_1 = 0$), we can use eqn. (S30) to derive a simple expression for the intra-cavity field

$$a_1 = \frac{-\sqrt{\kappa_1^{\text{ext}}}\alpha_p}{i\delta - \frac{\kappa_1}{2} + \frac{g_m^2}{-i\delta + \Gamma_m/2}} \tag{S33}$$

Since $\Gamma_m \ll \kappa_1$ in our experiments, we get the following spectrum for the intra-cavity Stokes (a_1) near the phonon resonance (i.e., $\Omega \approx \Omega_m$)

$$\begin{aligned} a_1(\delta) &\simeq \frac{2(i\delta - \Gamma_m/2)\sqrt{k_1^{\text{ext}}}/\kappa_1 \alpha_p}{i\delta - \frac{\Gamma_m}{2}(1 - C)} \\ a_1(\Omega) &= \frac{2(i(\Omega_m - \Omega) - \Gamma_m/2)\sqrt{k_1^{\text{ext}}}/\kappa_1 \alpha_p}{i(\Omega_m - \Omega) - \frac{\Gamma_{\text{eff}}}{2}} \end{aligned} \tag{S34}$$

where $C = 4N_2|g_0^m|^2/(\kappa_1\Gamma_m)$ is the cooperativity, and $\Gamma_{\text{eff}} = \Gamma_m(1 - C)$ is effective acoustic linewidth. Without optomechanical coupling (i.e. $g_m = 0$), we see that the peak intra-cavity field is given by

$$a_1'(\Omega_m) = 2\frac{\sqrt{\kappa_1^{\text{ext}}}}{\kappa_1}\alpha_p \tag{S35}$$

However, with optomechanical coupling the intra-cavity field on resonance is given by

$$a_1(\Omega_m) = 2\frac{\sqrt{\kappa_1^{\text{ext}}}}{\kappa_1(1 - C)}\alpha_p \tag{S36}$$

Therefore, the relative peak height of the OMIA spectrum

$$\left| \frac{a_1(\Omega_m)}{a_1'(\Omega_m)} \right|^2 = \frac{1}{(1 - C)^2} \tag{S37}$$

can be used to directly measure the value of cooperativity (C) in our optomechanical system.

Section S4. Optomechanically induced transparency (OMIT)

In this section, we follow the approach outlined in Ref. [44] to derive the intra-cavity optical spectrum during OMIT measurements. The Hamiltonian of our optomechanical system that accounts for the external drive fields (i.e.,

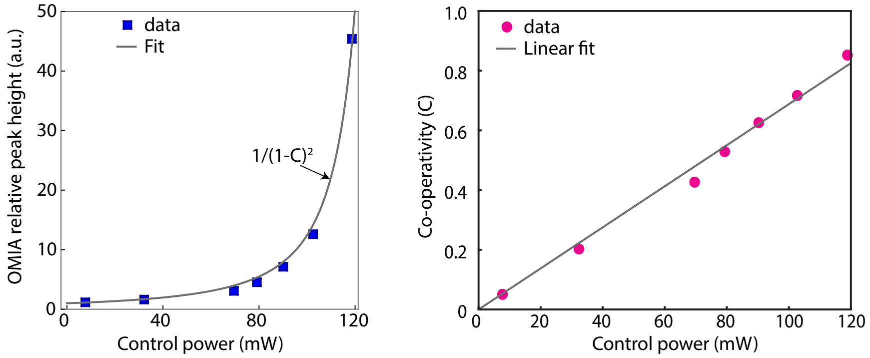

Fig. S6.OMIA measurement. a, The relative peak height of the OMIA signal increases non-linearly with the input control laser power. This increase matches well with the theoretically predicted $1/(1-C)^2$ dependency **b**, We use the measured relative peak height of the OMIA signal to calculate cooperativity C as a function of input control laser power. We use linear fit along with the values of optical and acoustic dissipation rates in Table S1 and N_2 obtained by measuring P_{in} to determine the single photon coupling rate $g_o^m/2\pi \simeq 18$ Hz.

the control laser and the probe laser) is given by

$$\begin{aligned} H = {}& \hbar\omega_1 a_1^\dagger \hat{a}_1 + \hbar\omega_2 a_2^\dagger a_2 + \hbar\Omega_m b_m^\dagger b_m - \hbar g_0^m (a_2^\dagger a_1 b_m + b_m^\dagger a_1^\dagger a_2) \\ & + i\hbar\sqrt{\kappa_1^{\text{ext}}}\alpha_l (a_1^\dagger e^{-i\omega_l t} - a_1 e^{i\omega_l t}) + i\hbar\sqrt{\kappa_2^{\text{ext}}}\alpha_p (a_2^\dagger e^{-i\omega_p t} - a_2 e^{i\omega_p t}) \end{aligned} \tag{S38}$$

Note that we normalize the incident optical power launched into the cavity such that $P_l = \hbar\omega_l \langle \alpha_l^\dagger \alpha_l \rangle$. We assume a strong control laser and a weak probe; within the undepleted pump approximation, the dynamics of the mode at frequency ω_1 is not influenced by the optomechanical coupling and it can be described by the following equation of motion derived from the Hamiltonian in eqn. (S38)

$$\dot{a}_1(t) = \left(-i\omega_1 - \frac{\kappa_1}{2}\right) a_1 + \sqrt{\kappa_1^{\text{ext}}}\alpha_l e^{-i\omega_l t} \tag{S39}$$

where $\kappa_1 = 2\kappa_1^{\text{ext}} + \kappa_1^0$, κ_1^{ext} is the loss rate at each cavity mirror and k_1^0 is the loss rate inside the cavity. From eqn. (S39), we obtain the following steady state solution for mode a_1

$$\langle a_1 \rangle = \sqrt{N_1} e^{-i\omega_l t} = \left| \frac{\sqrt{\kappa_1^{\text{ext}}}\alpha_l}{i\Delta_1 + \kappa_1/2} \right| e^{-i\omega_l t} \tag{S40}$$

where N_1 is the control laser driven intra-cavity photon number for mode a_1, and $\Delta_1 = \omega_1 - \omega_l$. (see fig. S5). Once we know the intra-cavity photon number for mode a_1, we can use input-output formalism for a symmetric Fabry-Pérot cavity, assuming laser fields incident only on one of the mirrors, to obtain the transmitted light field

$$a_{1,\text{out}} = \sqrt{\kappa_1^{\text{ext}}} a_1 \tag{S41}$$

In the undepleted pump regime, we substitute $\langle a_1 \rangle$ in eqn. (S38) to derive the following linearized Hamiltonian for the interaction between the optical mode a_2 and the phonon mode b_m

$$H = \hbar\omega_2 a_2^\dagger a_2 + \hbar\Omega_m b_m^\dagger b_m - \hbar g_0^m \sqrt{N_1}(a_2^\dagger b_m e^{-i\omega_l t} + b_m^\dagger a_2 e^{i\omega_l t}) + i\hbar\sqrt{\kappa_2^{\text{ext}}}\alpha_p (a_2^\dagger e^{-i\omega_p t} - a_2 e^{i\omega_p t}) \tag{S42}$$

From this Hamiltonian, by rotating in the frame of $H_0 = \hbar(\omega_p - \omega_l) b_m^\dagger b_m + \hbar\omega_p a_2^\dagger a_2$ (i.e. $a_2(t) \rightarrow a_2(t) e^{-i\omega_p t}$ and $b_m(t) \rightarrow b_m(t) e^{-i(\omega_l - \omega_p)t}$), we obtain an effective Hamiltonian

$$H_{\text{eff}} = -\hbar\delta b_m^\dagger b_m - \hbar(\delta + \Delta_2) a_2^\dagger a_2 - \hbar g_m (a_2^\dagger b_m + b_m^\dagger a_2) + i\hbar\sqrt{\kappa_2^{\text{ext}}}\alpha_p (a_2^\dagger - a_2) \tag{S43}$$

where $\delta = \Omega - \Omega_m = \omega_p - \omega_l - \Omega_a$, and $\Delta_2 = \Omega_a + \omega_l - \omega_2$, and the cavity field-enhanced coupling rate $g_m = g_0^m \sqrt{N_1}$. The Heisenberg equations of motions derived from this Hamiltonian, given by

$$\dot{a}_2(t) = \left(i(\delta + \Delta_2) - \frac{\kappa_2}{2}\right) a_2 + i g_m b_m + \sqrt{\kappa_2^{\text{ext}}}\alpha_p \tag{S44}$$

$$\dot{b}_m(t) = \left(i\delta - \frac{\Gamma_m}{2}\right) b + i g_m a_2 \tag{S45}$$

can be used to derive steady state values for the phonon and photon numbers

$$b_m = \frac{-ig_m}{\left(i\delta - \frac{\Gamma_m}{2}\right)} a_2 \tag{S46}$$

$$a_2 = \frac{-\sqrt{\kappa_2^{\text{ext}}}\alpha_p}{i(\delta + \Delta_2) - \frac{\kappa_2}{2} + \frac{g_m^2}{i\delta - \Gamma_m/2}} \tag{S47}$$

As before, we can use the input-output formalism to obtain the transmitted probe light given by

$$a_{2,\text{out}} = \sqrt{\kappa_2^{\text{ext}}} a_2 = -\frac{\kappa_2^{\text{ext}}\alpha_p}{i(\delta + \Delta_2) - \frac{\kappa_2}{2} + \frac{g_m^2}{i\delta - \Gamma_m/2}} \tag{S48}$$

In experiments, we use heterodyne detection of the transmitted probe light to measure the intra-cavity photon number. The power spectrum of this heterodyne signal at the detector is given by

$$P_d(\delta) \propto \langle a_{2,\text{out}}^\dagger a_{2,\text{out}} \rangle = \left| \frac{\kappa_2^{\text{ext}}}{i(\delta + \Delta_2) - \frac{\kappa_2}{2} + \frac{g_m^2}{i\delta - \Gamma_m/2}} \right|^2 \tag{S49}$$

If we assume that the frequency difference between the optical modes is exactly equal to the Brillouin frequency ($\omega_2 - \omega_1 = \Omega_m$) and the control laser is directly on resonance with the optical cavity mode a_1 ($\Delta_2 = 0$), we can use eqn. (S47) to derive a simple expression for the intra-cavity field

$$a_2 = \frac{-\sqrt{\kappa_2^{\text{ext}}}\alpha_p}{i\delta - \frac{\kappa_2}{2} + \frac{g_m^2}{i\delta - \Gamma_m/2}} \tag{S50}$$

Since $\Gamma_m \ll \kappa_2$ in our experiments, we get the following spectrum for the intra-cavity anti-Stokes (a2) near the phonon resonance (i.e., $\Omega \approx \Omega_m$)

$$\begin{aligned} a_2(\delta) &\simeq \frac{2(i\delta - \Gamma_m/2)\sqrt{k_2^{\text{ext}}}/\kappa_2\alpha_p}{i\delta - \frac{\Gamma_m}{2}(1 + C)} \\ a_2(\Omega) &= \frac{2(i(\Omega - \Omega_m) - \Gamma_m/2)\sqrt{k_2^{\text{ext}}}/\kappa_2\alpha_p}{i(\Omega - \Omega_m) - \frac{\Gamma_{\text{eff}}}{2}} \end{aligned} \tag{S51}$$

where $C = 4|g_0^m|^2 N_1/(\kappa_2\Gamma_m)$ is the multi-photon cooperativity, and $\Gamma_{\text{eff}} = \Gamma_m(1 + C)$ is effective phonon linewidth. Without optomechanical coupling (i.e. $g_m = 0$), we see that the peak intra-cavity field is given by

$$a_2'(\Omega_m) = 2\frac{\sqrt{\kappa_2^{\text{ext}}}}{\kappa_2}\alpha_p \tag{S52}$$

However, with optomechanical coupling the intra-cavity field on resonance is given by

$$a_2(\Omega_m) = 2\frac{\sqrt{\kappa_2^{\text{ext}}}}{\kappa_2(1 + C)}\alpha_p \tag{S53}$$

Therefore, the relative dip in the OMIT spectrum which is given by

$$\left| \frac{a_2(\Omega_m)}{a_2'(\Omega_m)} \right|^2 = \frac{1}{(1 + C)^2} \tag{S54}$$

can be used to directly measure the value of multi-photon cooperativity (C) in our optomechanical system.

Section S5. Acoustic diffraction loss

In this section, we first estimate the diffraction losses for our flat-flat resonator assuming the ideal case of no tilt misalignment between the optical cavity axis and the crystal axis. We use the approach outlined in Ref. [4], to determine diffraction losses in our system. The acoustic modes of our cylindrical resonator (see fig. S7 a) are given by

$$u_{m,k}(\mathbf{x}) = \beta_{m,k} \cos\left(\frac{m\pi z}{L_{\text{ac}}}\right) J_0\left(\frac{2j_{0,k}r}{d_c}\right) \tag{S55}$$

where J_0 is the zeroth order Bessel function of the first kind, $j_{0,k}$ is the k^{th} root of J_0, L_{ac} is the thickness of the crystalline resonator and d_c is the diameter of the quartz crystal, and $\beta_{m,k}$ is the normalization constant so that the total energy in each mode is equal to $\hbar\omega_{m,k}$. The frequency of each mode depends on the longitudinal mode number m and the transverse mode number k in the following way

$$\omega_{m,k} = \sqrt{\left(\frac{m\pi}{L_{\text{ac}}}\right)^2 v_l^2 + \left(\frac{2j_{0,k}}{d_c}\right)^2 v_t^2} \tag{S56}$$

where v_l is the longitudinal sound velocity and v_t is the effective transverse sound velocity. The acoustic field in our system is optically driven through electrostrictive force, which is proportional to the square of the electric field. The optical fields for the modes of our interest are Gaussian fields with transverse area that is essentially unchanging inside the crystal. Therefore, force profile due to optical driving is also Gaussian. To calculate diffraction of the phonons that start at some initial profile $u_0(\mathbf{x}, t = 0)$ but evolve to $u(\mathbf{x}, t)$ after some time t, we use the eigenmode expansion as

$$u(\mathbf{x}, t) = \sum_{m',k'} c_{m',k'} e^{-i\omega_{m',k'}t} u_{m',k'}(\mathbf{x}) \tag{S57}$$

where the constant $c_{m',k'}$s are determined from the initial displacement profile due to the electrostrictive driving given by

$$u_0(\mathbf{x}, t = 0) = U_0 \cos\left(\frac{m\pi z}{L_{ac}}\right) e^{-2r^2/w_{\text{opt}}^2} \tag{S58}$$

where w_{opt} is the waist of the optical Gaussian beam that drives the phonon modes. To calculate diffraction losses we calculate the overlap of the phonon field at time t with the original state $u_0(\mathbf{x}, t = 0)$. In particular we look at

$$|\eta(t)|^2 = |\langle u(\mathbf{x}, t)|u(\mathbf{x}, t = 0)\rangle|^2 \tag{S59}$$

$$= \left|\sum_{k'} |c_{m,k'}|^2 e^{i\omega_{m,k'}t}\right|^2 \tag{S60}$$

We obtain the acoustic energy lost from diffraction by plotting the normalized value of $|\eta(t)|^2$ (i.e.$|\eta(t)|^2/|\eta(t = 0)|^2$) as a function of time (see fig. S7 b). Fitting an exponential to this plot, we get an order of magnitude estimate for the decay time ~ 17 μs, which corresponds to phonon linewidth $\Gamma_m/2\pi = 9$ kHz.

In experiments, however, we measure a linewidth ($\Gamma_m/2\pi = 86$ kHz) that is much larger than the diffraction loss limit of 9 kHz. Note that for the diffraction loss calculation, we assumed that there is no tilt misalignment between the optical cavity axis and the crystal axis. Phonons encounter additional diffractive losses in the planar acoustic geometry if the crystal axis is tilted with respect to the optical cavity axis (see fig. S7 c). This is analogous to the well known losses introduced by tilting a Fabry-Pérot etalon inside an optical cavity (see Ref. [45]).

The measured finesse of our acoustic cavity was about 7. We calculate that even a small tilt angle of 0.07 degree is enough to result in lateral offset for the Gaussian acoustic beam that is twice the initial acoustic waist after 7 round-trips. Since the crystal is sitting on the Invar holder, whose surfaces are not perfectly flat, it is entirely possible in our experiment to have this level of misalignment. By designing a stable plano-convex acoustic cavity it is possible to mitigate the effects of diffraction and make the acoustic loss less sensitive to tilt misalignment.

Acoustic Q-factor of 4 $2.\times 10^7$ ($\Gamma_m \approx 2\pi \times 300$ Hz) has already been demonstrated for 12.7 GHz phonons confined within such plano-convex quartz resonators at cryogenic temperatures (~ 10 K) (see Ref. [24]). It is intriguing to consider using such highly coherent phonons to access, control, and study defect centers (or Two Level Systems (TLS)) in a variety of materials (see Ref. [36-37]). Using such high-Q resonators fabricated on-chip (see Ref. [25]), it is possible to create phonon modes with mode volumes of $\sim 1.6\times10^{-13}$ m^3 having zero-point strain fields $S = q \times x_{\text{zpf}} \approx 1.5\times10^{-11}$, where q is the acoustic wavevector and x_{zpf} is the zero-point amplitude of the acoustic displacement field (see Eq. S10). Assuming a deformation potential of 1 eV per unit strain for a single TLS, we estimate zero-point strain induced frequency shift of TLS energy level of about 4 kHz. Note than this zero-point coupling rate for phonon-TLS interaction is more than 10 times larger than acoustic cavity linewidth. Therefore, utilizing defect centers that have very long lifetimes at cryogenic temperatures (see Ref. [46]), it may be possible to enter strong coupling regime for phonon-TLS interaction. Such regime would allow phononic access to defect centers for scientific studies of phononic decoherence mechanisms as well as for quantum acoustic technologies.

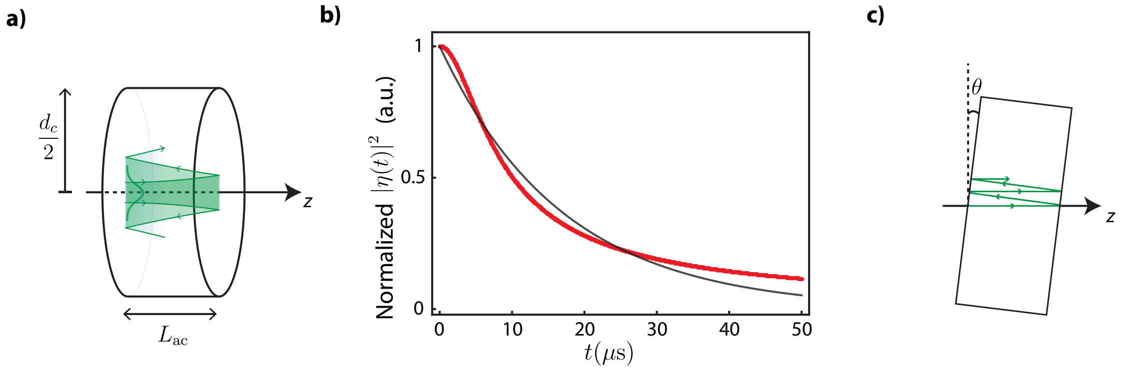

Fig. S7.Acoustic diffraction loss. **a**, Our acoustic resonator has a cylindrical geometry, with $L_{\text{ac}} = 5.19$ mm and $d_c = 12.7$ mm. Gaussian acoustic beam diffracts upon propagation inside the crystalline medium resulting in loss of acoustic energy. **b**, We obtain a diffraction loss limited lifetime of $\sim 17\mu\text{s}$, which corresponds to a phonon linewidth of ~ 9 kHz. For this calculation of acoustic diffraction loss we used the following parameters: $\text{w}_{\text{opt}} = 61$ μm, $\text{w}_{\text{ac}} = 43$ μm, $v_l = 6319$ m/s, $v_t = 5112$ m/s, and $\Omega_m/2\pi = 12.645$ GHz. **c**, Even a small tilt angle (θ) of the crystal axis with respect to the acoustic axis can result in a large spatial walk-off of the phonon beam resulting in diffractive losses.

Section S6. Thermal fluctuations and phonon lasing

In this section, we look at the power spectrum of the spontaneously scattered Stokes light due to thermal fluctuations of our mechanical mode. We consider the case where the control laser in directly on resonance with the high-frequency optical mode ($\omega_l = \omega_2$) and the frequency spacing between the two adjacent optical modes is equal to the Brillouin frequency ($\omega_2 - \omega_1 = \Omega_m$).

For measurements of thermal fluctuations we turn off the probe laser ($\alpha_p = 0$). Starting with the Hamiltonian from eqn. (S21) and setting $\alpha_p = 0$, we obtain

$$\begin{aligned} H = {} & \hbar\omega_1 a_1^\dagger \hat{a}_1 + \hbar\omega_2 a_2^\dagger a_2 + \hbar\Omega_m b_m^\dagger b_m - \hbar g_0^m (a_2^\dagger a_1 b_m + b_m^\dagger a_1^\dagger a_2) \\ & + i\hbar\sqrt{\kappa_2^{\text{ext}}}\alpha_l (a_2^\dagger e^{-i\omega_2 t} - a_2 e^{i\omega_2 t}) \end{aligned} \tag{S61}$$

As before, we assume a strong control laser and weak optomechanical coupling to derive the following steady state amplitude for mode a_2

$$\langle a_2 \rangle = \sqrt{N_2} e^{-i\omega_l t} = 2\frac{\sqrt{\kappa_2^{\text{ext}}}}{\kappa_2}\alpha_l e^{-i\omega_2 t} \tag{S62}$$

where N_2 is the intra-cavity photon number in mode a_2. We substitute $\langle a_2 \rangle$ into the Hamiltonian in eqn. (S61) and by rotating in the frame of the control laser (i.e. $a_2(t) \to a_2(t)e^{-i\omega_2 t}$), we obtain the following linearized Hamiltonian

$$H_{\text{eff}} = -\hbar\Omega_m a_1^\dagger a_1 + \hbar\Omega_m b_m^\dagger b_m - \hbar g_m (a_1 b_m + b_m^\dagger a_1^\dagger) \tag{S63}$$

where $g_m = \sqrt{N_2} g_0^m$ is the cavity-enhanced optomechanical coupling rate. The Heisenberg-Langevin equations of motion derived from this effective Hamiltonian are

$$\dot{a}_1 = \left(i\Omega_m - \frac{\kappa_1}{2}\right) a_1 + i g_m b_m^\dagger \tag{S64}$$

$$\dot{b}_m = \left(-i\Omega_m - \frac{\Gamma_m}{2}\right) b_m + i g_m a_1^\dagger + \sqrt{\Gamma_m}\tilde{b}_{\text{in}} \tag{S65}$$

where $\tilde{b}_{\text{in}}(t)$ is the input thermal fluctuation that drives the phonon mode. We assume a Markovian noise process (see Ref. [15]) such that

$$\langle \tilde{b}_{\text{in}}^\dagger(t)\tilde{b}_{\text{in}}(t')\rangle = n_{\text{th}}\delta(t - t') \tag{S66}$$

$$\langle \tilde{b}_{\text{in}}(t)\tilde{b}_{\text{in}}^\dagger(t')\rangle = (n_{\text{th}} + 1)\delta(t - t') \tag{S67}$$

$\langle \ldots \rangle$ represents an ensemble average, and $n_{\rm th} = (e^{\hbar\Omega_m/k_B T} - 1)^{-1}$ denotes the average number of thermal phonons of angular frequency Ω_m at temperature T. For instance, at a temperatures of 10 Kelvin, $n_{\rm th} \simeq 16$ for 12.645 GHz phonon modes. In contrast, the optical fields have essentially zero thermal occupation even at room temperatures since they are at much higher frequencies (~ 200 THz). Therefore, we ignore thermal fluctuations of the optical field in our calculations. Furthermore, we assume that the externally driven laser source is a pure coherent tone (no added noise from the laser itself), which is a good approximation for our experiments.

We now use Fourier-transform (defined as $f(\omega) = \int_{-\infty}^{+\infty} dt\ f(t)e^{i\omega t}$) to solve eqns. (S64-S65) in frequency space, which are given by

$$a_1(\omega) = \frac{-ig_m}{i(\omega+\Omega_m) - \kappa_1/2} b_m^\dagger(\omega) \tag{S68}$$

$$b_m(\omega) = \frac{i\sqrt{\Gamma_m}}{(\omega - \Omega_m + i\Gamma_m/2 + \Sigma(\omega))} \tilde{b}_{\rm in}(\omega) \tag{S69}$$

where we define

$$\Sigma(\omega) = \delta\Omega_m(\omega) - i\frac{\Gamma_{\rm opt}(\omega)}{2} = \frac{ig_m^2}{i(\omega - \Omega_m) - \kappa_1/2} \tag{S70}$$

Here, $\delta\Omega_m(\omega) = {\rm Re}\{\Sigma(\omega)\}$ gives us the frequency shift of the phonon mode and $\Gamma_{\rm opt}(\omega) = -2{\rm Im}\{\Sigma(\omega)\}$ gives us the optomechanical amplification rate. While $\Sigma(\omega)$ is frequency dependent, for weak coupling ($g_m \ll \kappa_1$), we can just evaluate $\delta\Omega_m(\omega)$ and $\Gamma_{\rm opt}(\omega)$ at $\omega = \Omega_m$ (see Ref. [15]). This calculation gives $\delta\Omega_m = 0$ and $\Gamma_{\rm opt} = 4g_m^2/\kappa_1$. So, we can re-write eqn. (S69) as

$$b_m(\omega) = \frac{i\sqrt{\Gamma_m}}{(\omega - \Omega_m + i\Gamma_m'/2)} \tilde{b}_{\rm in}(\omega) \tag{S71}$$

where $\Gamma_m' = \Gamma_m - \Gamma_{\rm opt} = \Gamma_m - 4g_m^2/\kappa_1$

We can use $b(\omega)$ in eqn. (S71) along with the noise correlations in eqns.(S66)-(S67) to calculate the power spectrum of laser driven mechanical mode, $S_{bb}(\omega)$, which is defined as

$$S_{bb}(\omega) = \int_{-\infty}^{+\infty} \langle b^\dagger(t) b(0)\rangle\, e^{i\omega t} dt \tag{S72}$$

$$= \frac{\Gamma_m n_{\rm th}}{(\omega + \Omega_m)^2 + (\Gamma_m'/2)^2} \tag{S73}$$

From this derivation we see that the power spectrum has a linewidth determined by the effective damping rate $\Gamma_m' = \Gamma_m(1 - \Gamma_{\rm opt}/\Gamma_m)$. Therefore, when the optomechanical amplification rate equals the cold cavity linewidth ($\Gamma_{\rm opt} = \Gamma_m$ or $C = \Gamma_{\rm opt}/\Gamma_m = 1$), a threshold condition is achieved, which leads to zero effective damping and regenerative self-oscillation of the phonon mode (also called phonon lasing).

We can also calculate the intra-cavity power spectrum of the spontaneously scattered light due to thermal fluctuations of the mechanical mode using eqns. (S68-S69). The power spectrum, $S_{a_1a_1}(\omega)$, is given by

$$S_{a_1a_1}(\omega) = \int_{-\infty}^{+\infty} \langle a_1^\dagger(t) a_1(0)\rangle\, e^{i\omega t} dt \tag{S74}$$

$$= \frac{g_m^2 \Gamma_m (n_{\rm th}+1)}{\left((\omega - \Omega_m)^2 + (\kappa_1/2)^2\right)\left((\omega - \Omega_m)^2 + (\Gamma_m'/2)^2\right)} \tag{S75}$$

From this expression we see that, using proper calibration of the heterodyne power spectrum of the spontaneously scattered light and values of g_m, Γ_m, κ_1 determined independently from the coherent (OMIA) measurements, it is possible to estimate the thermal phonon number in our system.

A. Slope efficiency

Once self-oscillating (i.e. above threshold) the total Stokes power as a function of input control power is given by (see supplementary materials of Ref. [47])

$$P_s \approx \frac{\kappa_p \omega_s v_p}{2\kappa_s \omega_p v_s}(P_{\rm in} - P_{\rm th}) \tag{S76}$$

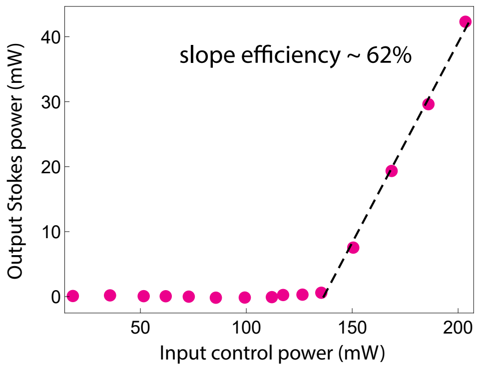

Fig. S8.Slope efficiency of the phonon laser. The backscattered optical power is used to determine total output Stokes power as a function of the input control laser power. This measurement reveals a slope efficiency of ≈ 62%, which is consistent with the theoretically estimated value of 57%.

where $\kappa_p(\kappa_s)$ is the optical cavity linewidth, $v_p(v_s)$ is the group velocity of optical mode at frequency $\omega_p(\omega_s)$ respectively, and P_{th} is the threshold input power for self-oscillation. Using the parameters from table S1 we calculate the slope efficiency $P_s/(P_{\text{in}} - P_{\text{th}}) \approx 57\%$. This agrees well with the experimentally measured value of 62 % (see fig. S8).

B. Phonon laser linewidth

Next we estimate the quantum-back-action limited linewidth and phase noise of our phonon laser. At $C = 1.4$, from the measurements of backreflected optical power, we estimate total scattered output Stokes power of $P_s = 42$ mW (see fig. S8). Knowing the scattering rate of Stokes light per phonon, $\gamma_{\text{ OM}} = 4G^2/\kappa$, we can calculate the steady state coherent phonon number as

$$n_c = \frac{P_s}{\hbar\omega\gamma_{\text{OM}}} = 4.2 \times 10^{11} \tag{S77}$$

This large coherent phonon number should produce dramatic Schawlow-Townes narrowed linewidth (see Ref. [48]) given by

$$\Delta\Omega = \frac{\Gamma_m}{2n_c}(n_{\text{th}} + 1) = 2\pi \times 1.7 \text{ µHz} \tag{S78}$$

where $n_{\text{th}} = 16$ at 10 Kelvin temperatures. Such ultra-narrow linewidth would result in a phase noise of -145 dBc/Hz at 10 KHz offset for a 12.6 GHz opto-mechanical oscillator. Dramatic improvement in the quantum-back-action limited phase noise performance is possible within this quartz optomechanical system by using a plano-convex acoustic resonator having an intrinsic phonon dissipation rate $\Gamma_m = 2\pi \times 300$ Hz (see Ref. [24]). For similar control input laser powers of 204 mW, we obtain steady state phonon population of 2×10^{12}. This would result in a Schawlow-Townes narrowed linewidth of $\Delta\Omega = 2\pi \times 0.5$ nHz at 4 Kelvin temperature. Such highly coherent oscillator would have a phase noise of -181 dBc/Hz at 10 kHz offset for a 12.7 GHz optomechanical oscillator.

Section S7. Relative scattering rate

In this section, we calculate the scattering rate difference between the Stokes and anti-Stokes processes for our multi-mode optomechanical system. In a single-mode optomechanical system, a control laser is typically detuned from an optical resonance by Ω_m to achieve a large difference in the Stokes and the anti-Stokes scattering rate (provided that $\Omega_m \gg \kappa$). However, the coherent driving field is directly on resonance with an optical mode in our optomechanical system. Nevertheless, we can engineer large asymmetry in the scattering rates for the Stokes and the anti-Stokes processes by engineering the optical density of states.

To explore this we consider a Hamiltonian that describes three optical modes interacting with a single phonon mode

$$H = \sum_{j=0,1,2} \hbar\omega_j a_j^\dagger a_j + \hbar\Omega_m b_m^\dagger b_m - \hbar g_{0,-}^m (a_1^\dagger a_0 b_m + b_m^\dagger a_0^\dagger a_1) - \hbar g_{0,+}^m (a_2^\dagger a_1 b_m + b_m^\dagger a_1^\dagger a_2) + H_{\text{drive}} \tag{S79}$$

Here, a_j (b_m) is the annihilation operator for the optical (phonon) mode at frequency ω_j (Ω_m), $g^m_{0,\mp}$ is the single photon coupling rate for the Stokes (anti-Stokes) scattering processes, and H_{drive} is the Hamiltonian for the external drive field. Since all the fundamental longitudinal optical modes considered here have essentially the same mode profiles $g_{0,+} = g_{0,-} = g^m_0$ is an excellent approximation.

For our calculation, we assume that the coherent laser field is driving the optical mode at frequency ω_1 directly on resonance ($\omega_l = \omega_1$). We also assume that only two optical modes (a_1 and a_2) are frequency separated by the phonon frequency ($\omega_2 - \omega_1 = \Omega_m$). Then, $\omega_1 - \omega_0 = \Omega_m + \chi$, where χ characterizes the asymmetry in the optical FSR. We also assume that the decay rate of the optical modes is due to the external coupling loss due to finite reflectivity of the two mirrors ($\kappa_j = 2\kappa_{\text{ext}}$). For weak optomechanical coupling, we assume undepleted pump and a large coherent field amplitude $\langle a_1 \rangle = \sqrt{N_1} e^{-i\omega_1 t}$, where $\sqrt{N_1} = 2(\sqrt{\kappa_{\text{ext}}}/\kappa)\alpha_l$ and $P_{\text{in}} = \hbar\omega_1 \langle \alpha_l^\dagger \alpha_l \rangle$.

Working in the rotating frame of $H_0 = \hbar\omega_1 a_1^\dagger a_1$ (i.e. $a_1(t) \to a_1(t)e^{-i\omega_1 t}$), we obtain the following linearized Hamiltonian from eqn. (S79)

$$H_{\text{eff}} = -\hbar(\Omega_m + \chi)a_0^\dagger a_0 + \hbar\Omega_m a_2^\dagger a_2 - \hbar g_m(a_0 b_m + b_m^\dagger a_0^\dagger) - \hbar g_m(a_2^\dagger b_m + b_m^\dagger a_2) \tag{S80}$$

where $g_m = g^m_0\sqrt{N_1}$. We use this Hamiltonian to derive the following Heisenberg-Langevin equations of motion for the dynamics of the anti-Stokes photon, Stokes photon and the phonon

$$\dot{b}_m = \left(-i\Omega_m - \frac{\Gamma_m}{2}\right) b_m(t) + ig_m a_0^\dagger + ig_m a_2 + \sqrt{\Gamma_m}\tilde{b}_{\text{in}} \tag{S81}$$

$$\dot{a}_0 = \left(i(\Omega_m + \chi) - \frac{\kappa_0}{2}\right) a_0 + ig_m b_m^\dagger \tag{S82}$$

$$\dot{a}_2 = \left(-i\Omega_m - \frac{\kappa_2}{2}\right) a_2(t) + ig_m b_m \tag{S83}$$

Using these equations we obtain the following equation for the phonon mode amplitude in frequency space:

$$b_m(\omega) = \frac{i\sqrt{\Gamma_m}\tilde{b}_{\text{in}}(\omega)}{(\omega - \Omega_m) + i\Gamma_m/2 + \Sigma^-(\omega) + \Sigma^+(\omega)} \tag{S84}$$

where the modification to the mechanical susceptibility due to optomechanical coupling is given by

$$\Sigma^-(\omega) = \delta\Omega^-_m(\omega) + i\frac{\Gamma_-(\omega)}{2} = \frac{ig_m^2}{i(\omega - \Omega_m - \chi) - \kappa_0/2} \tag{S85}$$

$$\Sigma^+(\omega) = \delta\Omega^+_m(\omega) + i\frac{\Gamma_+(\omega)}{2} = \frac{-ig_m^2}{i(\omega - \Omega_m) - \kappa_0/2} \tag{S86}$$

As discussed in Section VI, the real and imaginary parts of $\Sigma^\pm(\omega)$ determine mechanical frequency shift ($\delta\Omega^\pm_m(\omega)$) and the optomechanical damping/amplification rate ($\Gamma_\pm(\omega)$). For weak coupling $g_m \ll \kappa/2$ and $\Gamma_m \ll \kappa$, we can simply evaluate $\Sigma^\pm(\omega)$ at the mechanical frequency $\omega = \Omega_m$ to get

$$\delta\Omega^-_m = -\frac{g_m^2\chi}{\chi^2 + (\kappa_0/2)^2} \tag{S87}$$

$$\Gamma_- = -\frac{g_m^2\kappa_0}{\chi^2 + (\kappa_0/2)^2} \tag{S88}$$

$$\delta\Omega^-_m = 0, \tag{S89}$$

$$\Gamma_+ = \frac{4g_m^2}{\kappa_2} \tag{S90}$$

If we assume $\kappa_0 \simeq \kappa_2 = \kappa$ and $\chi \gg \kappa$, we obtain

$$\Gamma_- \simeq = -4\frac{g_m^2\kappa}{\chi^2} = -\Gamma_+\left(\frac{\kappa}{2\chi}\right)^2 \tag{S91}$$

Therefore, for the optomechanical cooling process that we considered here, the Stokes process (phonon mode heating) is smaller than the anti-Stokes process (phonon mode cooling) by a factor of $(\kappa/2\chi)^2$.

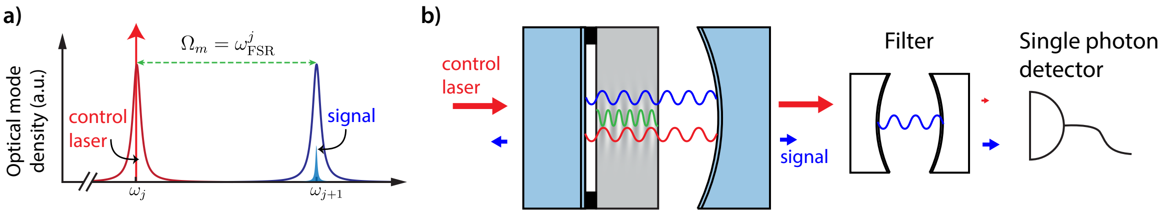

Fig. S9. Phonon counting in a multiresonant optomechanical system a, A strong control laser resonantly drives a lower frequency optical mode at frequency ω_j for phonon couting measurements. **b**, The transmitted light from this optomechanical system consists of both the signal (light scattered due to phonons) as well as the strong control laser, which must be filtered out before photon counting measurements.

Section S8. Phonon counting sensitivity

In this section, we derive phonon counting sensitivity in the weak coupling regime ($g_m \ll \kappa$) for our multi-mode optomechanical system and compare it with the phonon counting sensitivity for a single-mode optomechanical system presented in Ref. [17].

We use a strong coherent drive field that is directly resonant on the lower frequency optical mode ω_j while the probe laser ($\alpha_p = 0$) is turned off (see fig. S9a). We assume that $\omega_{\ j+1} - \omega_j = \Omega_m$. We use the following linearized Hamiltonian

$$H^{\mathrm{eff}} = \hbar\omega_{j+1} a^\dagger_{j+1} a_{j+1} + \hbar\Omega_m b^\dagger_m b_m - \hbar G(a^\dagger_{j+1} b_m e^{-i\omega_l t} + b^\dagger_m a_{j+1} e^{i\omega_l t}) \tag{S92}$$

to obtain Heisenberg equations of motion and use the input-output relations, to get the following relation for the high-frequency optical field exiting our optomechanical system

$$a_{\mathrm{out}}(t) = \sqrt{\kappa_e} a_{j+1}(t) \tag{S93}$$

$$\simeq \frac{2i\sqrt{\kappa_e} G b_m(t)}{\kappa} \tag{S94}$$

$$= i\sqrt{\frac{\kappa_e}{\kappa}}\sqrt{\gamma_{\mathrm{OM}}} b_m(t) \tag{S95}$$

where $G = \sqrt{n_c} g_0^m$ is the cavity enhanced coupling rate, κ_e is the external loss rate at each cavity mirror, $\kappa = 2\kappa_e$ is the total decay rate for each optical mode, and the optomechanical damping rate $\gamma_{\mathrm{OM}} = 4G^2/\kappa$. Since, $\langle a^\dagger_{\mathrm{out}} a_{\mathrm{out}} \rangle = (\kappa_e/\kappa)\gamma_{\mathrm{OM}} \langle b^\dagger_m b_m \rangle$, the rate of emission photons at frequency ω_{j+1} per phonon is $(\kappa_e/\kappa)\gamma_{\mathrm{OM}}$. These photons are detected with an overall system detection efficiency of η (this includes losses before the photon gets to the single photon detector as well as the less than unity detection efficiency of the single photon detector). The count rate per phonon on the detector due to our signal is $\Gamma_{\mathrm{sig}} = \eta(\kappa_e/\kappa)\gamma_{\mathrm{OM}}$.

In contrast to a single-mode optomechanical system, light transmitted through our multi-mode optomechanical system also has a large flux of control photons because the control laser is directly on resonance with the optical mode at ω_j. Assuming critical coupling and no internal losses, photon flux for the transmitted control laser in terms of the intra-cavity photon number is given by

$$\dot{N}_c = \frac{P_{\mathrm{in}}}{\hbar\omega} = \frac{n_c \kappa^2}{4\kappa_e} \tag{S96}$$

The transmitted light is passed through an additional optical filter to remove unwanted control laser (see fig. S9b) before photon detection. Let's assume an power attenuation of A. Then the count rate on the detector due to the wanted control laser is $\Gamma_{\mathrm{control}} = \eta A \dot{N}_c$.

So, the total count rate on the detector is given by

$$\Gamma_{\mathrm{tot}} = \Gamma_{\mathrm{sig}} \langle n \rangle + \Gamma_{\mathrm{control}} + \Gamma_{\mathrm{dark}} \tag{S97}$$

where $\langle n \rangle$ is the average phonon number and Γ_{dark} is the dark count rate of the signal photon detector.

To characterize the sensitivity of phonon counting we calculate the noise-equivalent phonon number for our multi-mode optomechanical system

$$\begin{aligned} n_{\mathrm{NEP}}^{\mathrm{MM}} &= n_{\mathrm{control}}^{\mathrm{MM}} + n_{\mathrm{dark}}^{\mathrm{MM}} \quad &\text{(S98)} \\ &= \frac{\Gamma_{\mathrm{control}} + \Gamma_{\mathrm{dark}}}{\Gamma_{\mathrm{sig}}} \quad &\text{(S99)} \\ &= A\left(\frac{\kappa^2}{4\kappa_e g_0}\right)^2 + \frac{\Gamma_{\mathrm{dark}}\kappa^2}{4\eta\kappa_e n_c {g_0}^2} \quad &\text{(S100)} \end{aligned}$$

For single phonon level sensitivity, we want $n_{\mathrm{NEP}} < 1$. In comparison, the noise-equivalent phonon number for a single-mode optomechanical system is given by (see Ref. [17])

$$\begin{aligned} n_{\mathrm{NEP}}^{\mathrm{SM}} &= n_{\mathrm{control}}^{\mathrm{SM}} + n_{\mathrm{dark}}^{\mathrm{SM}} \quad &\text{(S101)} \\ &= A\left(\frac{\kappa\Omega_m}{2\kappa_e g_0}\right)^2 + \frac{\Gamma_{\mathrm{dark}}\kappa^2}{4\eta\kappa_e n_c g_0^2} \quad &\text{(S102)} \end{aligned}$$

For same values of n_c, the expression for n_{dark} is the same for both multi-mode and single-mode optomechanical system. At experimentally achievable $\gamma_{\mathrm{OM}} > 1$ MHz and dark count rates of $\Gamma_{\mathrm{dark}} = 10$ Hz, $n_{\mathrm{dark}} \ll 1$.

Assuming symmetric Fabry-Pèrot type optomechanical system $(\kappa = 2\kappa_e)$, we find from eqn. (S98) and (S101) that

$$n_{\mathrm{control}}^{\mathrm{SM}} = A\left(\frac{\Omega_m}{g_0}\right)^2 \quad \text{(S103)}$$

$$n_{\mathrm{control}}^{\mathrm{MM}} = A\left(\frac{\kappa}{2g_0}\right)^2 \quad \text{(S104)}$$

From this we see that $n_{\mathrm{control}}^{\mathrm{MM}}$ is suppressed by the square of the optical finesse. However, $n_{\mathrm{control}}^{\mathrm{SM}}$ in a single-mode optomechanical system is independent of the optical finesse. Instead $n_{\mathrm{control}}^{\mathrm{SM}}$ increases as the square of the frequency of the phonon mode.

Note that the calculation we performed here is a conservative estimate because sensitivity can be enhanced by performing photon counting using the back-reflected light. When the control laser is critically coupled to our optomechanical cavity, back-reflected control laser power, in principle, is zero. In practice, we expect around 20 dB suppression of the unwanted counts from the control laser when using the back-reflection port.

Using a higher finesse optical cavity $(\mathcal{F} \approx 3000)$ with $\kappa/2\pi \simeq 4$ MHz and $g_0/2\pi \simeq 20$ Hz, we expect $n_{\mathrm{control}}^{\mathrm{MM}} < 1$ using 80 dB of filtering of the control laser in our multi-mode optomechanical system. In this system we get $\gamma_{\mathrm{OM}} = 2\pi \times 2$ MHz for $P_{\mathrm{in}} \approx 11$ mW. Assuming $\eta = 50\%$, we get $\Gamma_{\mathrm{sig}} = 2\pi \times 0.5$ MHz.